Available online at www.sciencedirect.com
ScienceDirect
Journal of Computational Physics 227 (2008) 8083–8106
JOURNAL OF COMPUTATIONAL PHYSICS
www.elsevier.com/locate/jcp

Domain reconstruction using photothermal techniques

Ana Carpio [a], María-Luisa Rapún [b,*]

[a] Dep. Matemática Aplicada, Fac. Matemáticas, Universidad Complutense de Madrid, 28040 Madrid, Spain
[b] Dep. Fundamentos Matemáticos, ETSI Aeronáuticos, Universidad Politécnica de Madrid, 28040 Madrid, Spain

Received 25 July 2007; received in revised form 11 March 2008; accepted 14 May 2008
Available online 9 July 2008

Abstract

A numerical method to detect objects buried in a medium by surface thermal measurements is presented. We propose a new approach combining the use of topological derivatives and Laplace transforms. The original optimization problem with time-dependent constraints is replaced by an equivalent problem with stationary constraints by means of Laplace transforms. The first step in the reconstruction scheme consists in discretizing the inversion formula to produce an approximate optimization problem with a finite set of constraints. Then, an explicit expression for the topological derivative of the approximate shape functional is given. This formula is evaluated at low cost using explicit expressions of the forward and adjoint fields involved. We apply this technique to a simple shape reconstruction problem set in a half space. Good approximations of the number, location and size of the obstacles are obtained. The description of their shapes can be improved by more expensive hybrid methods combining time averaging with topological derivative based iterative schemes.

PACS: 02.30.Zz; 02.60.Pn; 02.60.Lj; 65M32; 78A46

Keywords: Shape reconstruction; Nondestructive testing; Topological derivatives; Laplace transform; Boundary integral methods; Scattering; Heat equation; Thermal waves

1. Introduction

Photothermal techniques are becoming an effective tool in nondestructive testing of composite materials. Recent experiments aiming to reconstruct internal properties of materials are described in [14,26,30,32]. The goal is to detect structural defects or inclusions and determine their location, size, shape, orientation and physical properties. This is done by heating the exterior surface of the material using a defocused laser beam and measuring the temperature on the surface. Unlike acoustic waves, thermal waves are highly damped [23,27]. They are useful to obtain information near the surface. Applications to the recovery of dielectric coating factors or detection of corrosion are studied in [6,18]. The properties of thermal waves and their multiple

* Corresponding author. Tel.: +34 913363287.
E-mail addresses: ana_carpio@mat.ucm.es (A. Carpio), marialuisa.rapun@upm.es (M.-L. Rapún).

0021-9991/$ - see front matter © 2008 Elsevier Inc. All rights reserved.
doi:10.1016/j.jcp.2008.05.014

usages are discussed in [1,23,24,29]. We refer to [12,20] and references therein for theoretical results on inverse problems involving heat equations.

In this paper, we use thermal waves for the reconstruction of inclusions near the surface of a matrix. In [25] tomographic techniques relying on thermal waves are used to guess the shape of an inhomogeneity in a turbid medium. Further domain identification tests are carried out in [2,3,17]: an unknown part of a domain has to be reconstructed from measurements of the temperature in the known part. In [15], scatterers buried in a medium are detected by means of time-harmonic acoustic waves.

A common strategy in scattering problems consists in collecting data originated by time-harmonic waves arriving from several directions or sources at different frequencies. The scatterers buried in the medium must be reconstructed from such measurements. In our case, receptors can only be placed on the surface of the material and the set of possible incident directions is restricted. Reconstruction tests using time-harmonic incident waves produce poor results. We resort instead to general time-dependent sources. Handling time-harmonic excitations is simple, because we are left with stationary problems. More general incident waves lead to evolution problems.

A way to solve our inverse scattering problem consists in minimizing a shape functional with a constraint in the form of a transmission problem for a heat equation. We propose a strategy to approximate the scatterers based on the idea of topological derivative. Topological derivative methods have arisen as a powerful tool in imaging and nondestructive testing, see [7,8,11,13,15,16] and references therein for applications with time-harmonic sources. For general time-dependent sources, we might either compute the topological derivative of the time-dependent formulation or reduce the original problem to a family of optimization problems with stationary constraints by means of Laplace transforms and calculate the topological derivatives of the resulting functional. The first strategy is more expensive than the second one. At present, it does not seem to provide efficient schemes to reconstruct objects.

In this paper, we propose simple and efficient schemes generated by taking Laplace transforms in time and exploiting the topological derivative techniques developed for the time-harmonic case. Choosing carefully the inversion path for the Laplace transform [19,22], the resulting procedure is computationally efficient: only a small number of stationary forward and adjoint fields have to be computed. The topological derivatives are directly calculated using explicit expressions for these fields, which solve Helmholtz equations in the whole space. A judicious selection of sampling points and times improves the quality of the reconstructions. The cost of adding information coming from new measurements at different times is negligible. More precise descriptions of the shape of the obstacles are found by combining time recording with topological derivative based iterative techniques. These hybrid schemes use boundary integral methods to compute forward and adjoint fields in each iteration, which now solve unbounded transmission problems. The resulting schemes are more accurate, but also more expensive.

These strategies can be useful in other contexts requiring a knowledge of the time record. In medical applications, knowing the time-varying distribution of electrical properties inside a body is useful to differentiate between different tissues and locate blood clots or tumors [9]. In synthetic aperture radar, data are recorded during a certain time for general time-dependent electromagnetic signals, see [4].

The paper is organized as follows. Section 2 describes the forward scattering model in a half-space and reformulates the inverse problem as a constrained optimization problem. Section 3 starts with a short background on topological derivative methods applied to time-harmonic problems. These methods are then extended to functionals with time-dependent constraints using Laplace transforms and combined with topological derivative based iterative schemes. Numerical experiments comparing scattering by time-harmonic and more general time-dependent sources are presented in Section 4. Reasonable reconstructions are found at a low computational cost. Section 5 gives a formula for the time-dependent topological derivative and comments on the difficulties encountered when implementing schemes based on it. The derivation of the formulae for the topological derivative of the 'Laplace transformed' functional and the time-dependent functional are given in Appendixes A and B, respectively. Our conclusions are summarized in Section 6.

2. The time-dependent inverse problem

We consider a matrix Ω_e containing inclusions Ω_i of a different material near its surface. The whole composite medium is identified with $\mathbb{R}^n_- := \{(x_1,\ldots,x_n) \in \mathbb{R}^n,\ x_n \leqslant 0\},\ n = 2$ or 3. We wish to determine the

shape, size, topology and location of the inclusions in this semi-infinite medium from the temperature measured over a time interval on the surface of the sample Π, that has been thermically excited by an incident radiation U_{inc}. Recent experimental work on this technique can be found in [14,26,30].

The temperature of the system is governed by a diffusion model:

$$\begin{cases} U_t - \kappa_e \Delta U = 0 & \text{in } \Omega_e \times (0,\infty), \\ U_t - \alpha_i \kappa_i \Delta U = 0 & \text{in } \Omega_i \times (0,\infty), \\ U^- - U^+ = U_{\text{inc}} & \text{on } \Gamma \times (0,\infty), \\ \alpha_i \partial_{\mathbf{n}} U^- - \partial_{\mathbf{n}} U^+ = \partial_{\mathbf{n}} U_{\text{inc}} & \text{on } \Gamma \times (0,\infty), \\ \partial_{\mathbf{n}} U = 0 & \text{on } \Pi \times (0,\infty), \\ U(\cdot,0) = 0 & \text{in } \mathbb{R}^n_-, \end{cases} \tag{1}$$

where $\Omega_e := \mathbb{R}^n_- \setminus \overline{\Omega}_i$. Here U represents the scattered field in Ω_e and the transmitted field in Ω_i. The outward normal vector $\mathbf{n}$ points outside Ω_e. We denote by U^+ and U^- the limits of U from the exterior and interior of Ω_i, respectively, and $\partial_{\mathbf{n}}$ stands for the normal derivative. An adiabaticity condition is imposed on the upper boundary $\Pi := \{(x_1,\ldots,x_n) \in \mathbb{R}^n,\ x_n = 0\}$.

The parameter $\alpha_i > 0$ is the ratio of the interior and exterior thermal conductivities. The diffusivities of the materials are $\kappa_e,\ \alpha_i\kappa_i > 0$. We write $\alpha_i\kappa_i$ for the interior diffusivity because it simplifies the later computation of topological derivatives.

The domain $\Omega_i \subset \mathbb{R}^n_-$ is an open bounded set with smooth boundary $\Gamma := \partial\Omega_i$ but we do not assume connectivity. There may be an unknown number of isolated components, that is, $\Omega_i = \cup_{j=1}^d \Omega_{i,j}$ with $\Omega_{i,j}$ open connected bounded sets satisfying $\overline{\Omega}_{i,l} \cap \overline{\Omega}_{i,j} = \emptyset$ for $l \neq j$ (see Fig. 1).

Scattering patterns are measured at detector locations Γ_{meas} placed on Π. The sources are also located on Π. Time-harmonic excitations generated at a point $\mathbf{x}_0 \in \Pi$ take the form $U_{\text{inc}}(\mathbf{x},t) = \text{Re}(u_{\text{inc}}(\mathbf{x})e^{-i\omega t})$, where

$$u_{\text{inc}}(\mathbf{x}) := \phi_{\lambda_e}(\mathbf{x},\mathbf{x}_0), \tag{2}$$

ϕ_{λ_e} being the fundamental solution of the Helmholtz equation with wave-number λ_e

$$\phi_\lambda(\mathbf{x},\mathbf{y}) := \begin{cases} \frac{i}{4} H_0^{(1)}(\lambda|\mathbf{x}-\mathbf{y}|) & \text{if } n = 2, \\ \frac{\exp(i\lambda|\mathbf{x}-\mathbf{y}|)}{4\pi|\mathbf{x}-\mathbf{y}|} & \text{if } n = 3. \end{cases} \tag{3}$$

Time-dependent excitations of the form

$$U_{\text{inc}}(\mathbf{x},t) = \frac{1}{t^{\frac{n}{2}}} \exp\left(-\frac{|\mathbf{x}-\mathbf{x}_0|^2}{4\kappa_e t}\right), \quad \mathbf{x} \in \mathbb{R}^n,\ \ t > 0, \tag{4}$$

model a point source located at $\mathbf{x}_0$. In both cases, the incident wave satisfies the adiabaticity condition if the source point $\mathbf{x}_0$ is located on Π.

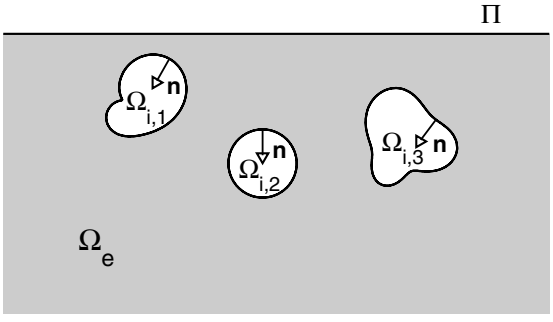

Fig. 1. Geometrical configuration: $\Omega_i = \cup_{j=1}^d \Omega_{i,j}$ and $\Omega_e = \mathbb{R}^n_- \setminus \overline{\Omega}_i$.

In practical experiments, the total field is known on a set of receptors Γ_{meas} placed on Π for a sequence of times. The inverse problem consists in finding the shape and structure of the obstacle Ω_i such that the solution of the forward transmission problem (1) equals the measured values $U_{\text{meas}}(\mathbf{x}, t_j)$ at the detector locations at times $t_1, \ldots, t_N$. This problem is ill-posed. Instead, we consider a weaker variational reformulation and seek a domain Ω_i solving a constrained optimization problem: minimize

$$J(\Omega_i) := \frac{1}{2} \sum_{j=1}^{N} f(t_j) \int_{\Gamma_{\text{meas}}} (U_{\text{total}}(\mathbf{x}, t_j) - U_{\text{meas}}(\mathbf{x}, t_j))^2 \mathrm{d}l_{\mathbf{x}}, \tag{5}$$

when $U_{\text{total}}(\mathbf{x}, t) = U(\mathbf{x}, t) + U_{\text{inc}}(\mathbf{x}, t)\chi_{\Omega_e}(\mathbf{x})$, $U(\mathbf{x}, t)$ being the solution of the forward problem (1). $\chi_{\Omega_e}(\mathbf{x})$ stands for the characteristic function of the domain Ω_e. On Γ_{meas}, $\chi_{\Omega_e} = 1$. The cost functional (5) depends on the design variable Ω_i through the heat equation, which acts as a constraint.

The positive weight function $f(t)$ accounts for the time decay of solutions of heat equations. The incident waves (4) are positive functions which decay with time. For $\mathbf{x} \neq \mathbf{x}_0$, they start from $U_{\text{inc}}(\mathbf{x}, 0) = 0$, attain a maximum at $t = |\mathbf{x} - \mathbf{x}_0|^2/(4\kappa_e n)$ and then decay to zero as time grows. The corresponding solution U of (1) shows a similar behavior. We will discuss different choices for f in Section 4.

Our choice of the boundary condition at the free surface Π allows to extend the original problem set in a half space to a problem set in the whole space by reflection. Let us denote by $\hat{\mathbf{x}}$ the reflected point of $\mathbf{x}$ with respect to Π, that is, $\hat{\mathbf{x}} = (x_1, x_2, -x_3)$ for $\mathbf{x} = (x_1, x_2, x_3) \in \mathbb{R}^3$ or $\hat{\mathbf{x}} = (x_1, -x_2)$ for $\mathbf{x} = (x_1, x_2) \in \mathbb{R}^2$. We define the symmetric domains

$$\widetilde{\Omega}_i := \Omega_i \cup \{\mathbf{x} \in \mathbb{R}^n,\ \hat{\mathbf{x}} \in \Omega_i\}, \quad \widetilde{\Omega}_e := \mathbb{R}^n \setminus \overline{\widetilde{\Omega}_i}$$

and the boundary $\widetilde{\Gamma} := \Gamma \cup \{\mathbf{x} \in \mathbb{R}^n,\ \hat{\mathbf{x}} \in \Gamma\}$. If U solves (1), then the reflected function

$$\widetilde{U}(\mathbf{x}, t) := \begin{cases} U(\mathbf{x}, t) & \text{if } \mathbf{x} \in \mathbb{R}^n_-, \\ U(\hat{\mathbf{x}}, t) & \text{if } \mathbf{x} \in \mathbb{R}^n \setminus \mathbb{R}^n_- \end{cases}$$

satisfies

$$\begin{cases} \widetilde{U}_t - \kappa_e \Delta \widetilde{U} = 0 & \text{in } \widetilde{\Omega}_e \times (0, \infty), \\ \widetilde{U}_t - \alpha_i \kappa_i \Delta \widetilde{U} = 0 & \text{in } \widetilde{\Omega}_i \times (0, \infty), \\ \widetilde{U}^- - \widetilde{U}^+ = \widetilde{U}_{\text{inc}} & \text{on } \widetilde{\Gamma} \times (0, \infty), \\ \alpha_i \partial_{\mathbf{n}} \widetilde{U}^- - \partial_{\mathbf{n}} \widetilde{U}^+ = \partial_{\mathbf{n}} \widetilde{U}_{\text{inc}} & \text{on } \widetilde{\Gamma} \times (0, \infty), \\ \widetilde{U}(\cdot, 0) = 0 & \text{in } \mathbb{R}^n, \end{cases} \tag{6}$$

where

$$\widetilde{U}_{\text{inc}}(\mathbf{x}, t) := \begin{cases} U_{\text{inc}}(\mathbf{x}, t) & \text{if } \mathbf{x} \in \mathbb{R}^n_-, \\ U_{\text{inc}}(\hat{\mathbf{x}}, t) & \text{if } \mathbf{x} \in \mathbb{R}^n \setminus \mathbb{R}^n_-. \end{cases}$$

Reciprocally, if $\widetilde{U}$ solves (6), the symmetry of the problem implies that $U := \widetilde{U}$ in $\mathbb{R}^n_-$ is a solution of (1). Green's function of the Helmholtz equation in the half space with wave-number λ and zero Neumann boundary condition on Π is

$$\phi_\lambda(\mathbf{x}, \mathbf{y}) + \phi_\lambda(\mathbf{x}, \widehat{\mathbf{y}}).$$

From now on, we will work indistinctly with solutions in the half space or their extensions to the whole space. For ease of notation, in the sequel U will be either the solution to (1) or to (6).

3. Topological derivatives for time-dependent problems: Laplace approach

In this section, we develop a topological derivative approach to solve inverse scattering problems reformulated as optimization problems with time-dependent constraints. The interested reader can find a formula for the topological derivative of the full time-dependent problem in Section 5, together with a discussion of the

difficulties encountered when trying to develop schemes based on it. This section is devoted to a hybrid Laplace transform–topological derivative approach, which works out nicely.

Let us first recall the definition of topological derivative of a shape functional. Consider a small ball $B_\varepsilon(\mathbf{x})$, $\mathbf{x} \in \mathcal{R}$, and the domain $\mathcal{R}_\varepsilon := \mathcal{R} \setminus \overline{B}_\varepsilon(\mathbf{x})$. For $\mathbf{x} \in \mathcal{R}$, the topological derivative of $\mathcal{J}(\mathcal{R})$ is

$$D_T(\mathbf{x}, \mathcal{R}) := \lim_{\varepsilon \to 0} \frac{\mathcal{J}(\mathcal{R}_\varepsilon) - \mathcal{J}(\mathcal{R})}{\mathcal{V}(\varepsilon)}, \tag{7}$$

where $\mathcal{V}(\varepsilon)$ is a positive function selected in such a way that the limit exists, is finite and does not vanish. In our case, $\mathcal{V}(\varepsilon) = \pi\varepsilon^2$ in 2D but $\mathcal{V}(\varepsilon) = \frac{4}{3}\pi\varepsilon^3$ in 3D.

The knowledge of the topological derivative of a shape functional is exploited to find information about the presence of obstacles as follows. Notice that its value depends on $\mathcal{R}$. When no a priori information on the set of scatterers Ω_i is available, we set $\mathcal{R} = \mathbb{R}^n$. Objects are likely to be located in the regions where $D_T(\mathbf{x}, \mathbb{R}^n)$ takes large negative values. In this way, a first guess Ω_i^1 for Ω_i is found. A guess Ω_i^k can be improved by setting $\mathcal{R} = \mathbb{R}^n \setminus \overline{\Omega}_i^k$ and adding to Ω_i^k the regions where the updated $D_T(\mathbf{x}, \mathcal{R})$ takes large negative values. The magnitude of the topological derivative decreases at each step and the updated guesses provide better reconstructions. This idea has been exploited to design iterative schemes to solve inverse scattering problems for time-harmonic sources [7,8].

In this section, we first study a simplified model with time-harmonic excitations. Afterwards, we deal with the full time-dependent problem, transforming it into a family of time-harmonic problems by means of Laplace transforms. The new shape functional is replaced by a discretized version with a finite set of stationary constraints. We compute the topological derivative of the discretized functional and use it to generate a first approximation to the set of scatterers. This approximation can be improved in two ways. First, by increasing the number of time recordings and selecting the times conveniently. This is a low cost strategy. Second, by a topological derivative based iterative scheme, which sharpens the reconstructions at a higher computational cost.

3.1. Time-harmonic problems

Incident fields of the form $U_{\text{inc}}(\mathbf{x}, t) = \text{Re}(u_{\text{inc}}(\mathbf{x})\text{e}^{-\imath\omega t})$ generate time-harmonic responses $U(\mathbf{x}, t) = \text{Re}(u(\mathbf{x})\text{e}^{-\imath\omega t})$ with frequency $\omega > 0$. The time-dependent problem becomes a stationary Helmholtz transmission problem and we may resort to standard topological derivative methods to find information on the structure of the material [7,8,16].

To be more precise, the functional to be optimized becomes

$$J(\Omega_i) := \frac{1}{2} \int_{\Gamma_{\text{meas}}} |u_{\text{total}} - u_{\text{meas}}|^2 \text{d}l \tag{8}$$

with $u_{\text{total}}(\mathbf{x}) = u(\mathbf{x}) + u_{\text{inc}}(\mathbf{x})$. Notice that we take the modulus of the difference $u_{\text{total}} - u_{\text{meas}}$, since both functions are complex-valued. The space-dependent amplitude of the scattered wave $u = u_{\text{sc}}$ in Ω_e, and of the transmitted wave $u = u_{\text{tr}}$ in Ω_i, solve the elliptic transmission problem

$$\begin{cases} \Delta u + \lambda_e^2 u = 0 & \text{in } \Omega_e, \\ \alpha_i \Delta u + \lambda_i^2 u = 0 & \text{in } \Omega_i, \\ u^- - u^+ = u_{\text{inc}} & \text{on } \Gamma, \\ \alpha_i \partial_{\mathbf{n}} u^- - \partial_{\mathbf{n}} u^+ = \partial_{\mathbf{n}} u_{\text{inc}} & \text{on } \Gamma \end{cases} \tag{9}$$

and satisfy the Sommerfeld radiation condition at infinity

$$\lim_{r \to \infty} r^{(n-1)/2}(\partial_r u - \imath\lambda_e u) = 0, \quad r = |\mathbf{x}|, \tag{10}$$

uniformly in all directions. The wave-numbers are $\lambda_\ell^2 = \imath\omega/\kappa_\ell$, $\ell = e, i$, that is, $\lambda_\ell = (1+\imath)\sqrt{\omega/(2\kappa_\ell)}$. Throughout this work, square roots of complex numbers are always taken with non-negative imaginary part. For our particular type of complex wave-numbers and $\alpha_i > 0$, problem (9) and (10) is always uniquely solvable (see [10] or [28]). Efficient numerical strategies to solve (9) and (10) by means of boundary element techniques are discussed in the survey [29].

Notice that the scattering of acoustic waves produces real and positive wave-numbers, whereas thermal waves give rise to Helmholtz problems with complex wave-numbers. Reconstruction strategies in the acoustic setting are discussed in [7,8,11,13,16] for either $\mathbb{R}^n$ or $\mathbb{R}^n_-$. With our choice of boundary conditions on the free surface Π, methods developed for the whole space apply in particular to half-spaces.

Below, we extend the known formula for the topological derivative of the functional (8) to the complex case. The generalization to complex wave-numbers requires only small adjustments.

Theorem 3.1. *The topological derivative of the cost functional (8) in $\mathbb{R}^n \setminus \overline{\Omega}_i$, $n = 2$ or 3, is given by*

$$D_T(\mathbf{x}, \mathbb{R}^n \setminus \overline{\Omega}_i) = \mathrm{Re}\left[\frac{n(1-\alpha_i)}{n-1+\alpha_i}\nabla u_{\mathrm{total}}(\mathbf{x})\nabla p(\mathbf{x}) + (\lambda_i^2 - \lambda_e^2)u_{\mathrm{total}}(\mathbf{x})p(\mathbf{x})\right] \tag{11}$$

for $\mathbf{x} \in \mathbb{R}^n \setminus \overline{\Omega}_i$. The state p is the continuous solution of

$$\begin{cases} \Delta p + \lambda_e^2 p = (\overline{u_{\mathrm{meas}} - u_{\mathrm{total}}})\delta_{\Gamma_{\mathrm{meas}}} & \text{in } \mathbb{R}^n \setminus \overline{\Omega}_i, \\ \alpha_i \Delta p + \lambda_i^2 p = 0 & \text{in } \Omega_i, \\ p^- - p^+ = 0 & \text{on } \Gamma, \\ \alpha_i \partial_{\mathbf{n}} p^- - \partial_{\mathbf{n}} p^+ = 0 & \text{on } \Gamma, \\ \lim\limits_{r\to\infty} r^{(n-1)/2}(\partial_r p - \imath\lambda_e p) = 0 & \end{cases} \tag{12}$$

and $u_{\mathrm{total}} = u_{\mathrm{inc}} + u$, where u solves (9) and (10). When $\Omega_i = \emptyset$, $u_{\mathrm{total}} = u_{\mathrm{inc}}$. The continuous solution of (12) is then:

$$p(\mathbf{x}) = -\int_{\Gamma_{\mathrm{meas}}} \phi_{\lambda_e}(\mathbf{x}, \mathbf{y})(\overline{u_{\mathrm{meas}}(\mathbf{y}) - u_{\mathrm{inc}}(\mathbf{y})})\mathrm{d}l_{\mathbf{y}}, \tag{13}$$

ϕ_{λ_e} being the fundamental solution of the Helmholtz equation (3).

Proof. In the two-dimensional case, the proofs of [7, Theorems 3.1 and 3.2], or [8, Theorems 1 and 2], for the real case can be followed step by step. The formula in three dimensions was obtained in [16] in a different way. Only real wave-numbers where considered in [7,8,16]. By revising the proofs, it is clear that the results remain valid for complex wave-numbers with a small change. The field p here is the conjugate of the adjoint state. The adjoint state $\bar{p}$ solves (12) replacing λ_ℓ^2 by $\overline{\lambda_\ell^2}$, $-\imath\lambda_\ell$ by $-\overline{\imath\lambda_\ell}$ for $\ell = e, i$, and removing the conjugate from the right-hand side. See Appendix A. □

3.2. Laplace-transformed problem

Let us consider now the evolution problem in the non-harmonic case. The original optimization problem with time-dependent constraints can be replaced by an approximate problem with stationary constraints by means of Laplace transforms. We describe below how this is accomplished. A rigorous justification for our transmission problem can be found in [21] (see also [29]). For related problems arising in the study of coated materials see [19].

Let U_{inc} be the incident field defined in (4) and U the corresponding solution of the time-dependent forward problem (6). We define then u_{inc} and u as the Laplace transforms in time of U_{inc} and U:

$$u_{\mathrm{inc}}(\mathbf{x}, s) = \int_0^\infty \mathrm{e}^{-st} U_{\mathrm{inc}}(\mathbf{x}, t)\mathrm{d}t, \quad u(\mathbf{x}, s) = \int_0^\infty \mathrm{e}^{-st} U(\mathbf{x}, t)\mathrm{d}t, \qquad \mathbf{x} \in \mathbb{R}^n.$$

For each value of s, the function $u_s(\mathbf{x}) := u(\mathbf{x}, s)$ solves

$$\begin{cases} \Delta u_s + \lambda_{s,e}^2 u_s = 0 & \text{in } \Omega_e, \\ \alpha_i \Delta u_s + \lambda_{s,i}^2 u_s = 0 & \text{in } \Omega_i, \\ u_s^- - u_s^+ = u_{\mathrm{inc},s} & \text{on } \Gamma, \\ \alpha_i \partial_{\mathbf{n}} u_s^- - \partial_{\mathbf{n}} u_s^+ = \partial_{\mathbf{n}} u_{\mathrm{inc},s} & \text{on } \Gamma, \end{cases} \tag{14}$$

where $\lambda_{s,e}^2 := -s/\kappa_e$, $\lambda_{s,i}^2 := -s/\kappa_i$ and $u_{\mathrm{inc},s}(\mathbf{x}) := u_{\mathrm{inc}}(\mathbf{x}, s)$. The Laplace transforms of our incident fields (4) are

$$u_{\mathrm{inc}}(\mathbf{x}, s) = \begin{cases} 2K_0\left(|\mathbf{x}-\mathbf{x}_0|\sqrt{s/\kappa_e}\right) & \text{if } n = 2, \\ \frac{2\sqrt{\pi\kappa_e}}{|\mathbf{x}-\mathbf{x}_0|}\exp\left(-|\mathbf{x}-\mathbf{x}_0|\sqrt{s/\kappa_e}\right) & \text{if } n = 3, \end{cases} \tag{15}$$

K_0 being the modified Bessel function of order zero. These expressions are valid for all $\mathbf{x} \in \mathbb{R}^n$, $\mathrm{Re}(s) > 0$, and admit holomorphic extensions to $s \in \mathbb{C} \setminus (-\infty, 0]$ (see [19, Lemma 10]).

Notice that problems (14) and (9) have the same structure. Problem (14) has a unique solution satisfying the Sommerfeld radiation condition at infinity

$$\lim_{r\to\infty} r^{(n-1)/2}(\partial_r u_s - \imath\lambda_{s,e}u_s) = 0, \quad r = |\mathbf{x}| \tag{16}$$

for all $s \in \mathbb{C} \setminus (-\infty, 0]$ (see for instance [10, Proposition 4.7]). This characterization of $u_s(\mathbf{x})$ can be used to define and compute $u(\cdot, s)$ for all $s \in \mathbb{C} \setminus (-\infty, 0]$.

The solution of the time-dependent problem (6) is recovered by inverting the Laplace transform:

$$U(\mathbf{x}, t) = \frac{1}{2\pi\imath}\int_{\mathcal{C}} \mathrm{e}^{st}u(\mathbf{x}, s)\mathrm{d}s.$$

Since $u(\cdot, s)$ exists for all $s \in \mathbb{C} \setminus (-\infty, 0]$ and depends holomorphically on s, many different choices for the inversion path $\mathcal{C}$ are possible, see [22,31]. Inverting the Laplace transform requires solving (14)–(16) for the values of s lying in the selected path. From a numerical point of view, the best paths are those along which this inversion formula can be accurately approximated by a quadrature formula involving as few points as possible.

The classical theoretical choice for inversion paths are Bromwich contours, which are parallel to the imaginary axis and are located to the right of the singularities of $u(\mathbf{x}, s)$. In this case, we may select the imaginary axis. The inversion formula holds if $u(\mathbf{x}, s) \to 0$ for $\mathrm{Re}(s) \geqslant 0$, $|s| \to \infty$ and $\int_{-\infty}^{\infty} |u(\mathbf{x}, \imath\omega)|\mathrm{d}\omega$ converges. For numerical purposes, the best choices of the inversion contour are based on deforming the standard Bromwich contour. A typical choice for problems where the Laplace transform is defined in $\mathbb{C} \setminus (-\infty, 0]$ and satisfies adequate decay conditions for large s are the Talbot contours (see [31]), which are asymptotically parallel to the negative real axis. From a computational point of view, hyperbolic paths are a better choice. A detailed analysis of the computational cost of inverting Laplace transforms using different paths is found in [22]. We choose the hyperbolic path that was proposed in [22], given by the parameterization $\gamma : \mathbb{R} \to \mathcal{C}$ with

$$\gamma(\theta) := \mu(1 - \sin(\beta + \imath\theta)), \quad \theta \in \mathbb{R},$$

where $\mu > 0$ and $0 < \beta < \pi/2$ are parameters that can be tuned to obtain an optimal performance of the method in the desired time interval. Then, U is computed as

$$U(\mathbf{x}, t) = \frac{1}{2\pi\imath}\int_{-\infty}^{\infty} \mathrm{e}^{t\gamma(\theta)}u(\mathbf{x}, \gamma(\theta))\gamma'(\theta)\mathrm{d}\theta. \tag{17}$$

We refer to [19] for guidelines on how to choose the parameters μ and β. In our numerical experiments we will take $\beta = \pi/4$ and adapt the value of μ depending on the values of t, in such a way that $\mu \approx 5/t$ as suggested in [19], where a rigorous justification of the fact that Laplace inversion formulae work for our transmission problem (6) is given.

As we will see in Section 3.3, a quadrature formula involving less than 21 nodes can be used to get a good approximation of the integral (17) with our choice of the inversion path. By symmetry, less than eleven stationary Helmholtz problems have to be solved. When $\Omega_i = \emptyset$, the solutions of the resulting Helmholtz equations are known explicitly. The cost of solving such stationary problems is negligible. When $\Omega_i \neq \emptyset$, none of the wave-numbers can be a Dirichlet eigenvalue of the Laplace operator in Ω_i, because they are complex. Therefore, problem (14)–(16) can be solved numerically at low cost by using elementary boundary integral formulations based on single layer potentials, as suggested in [28] (see also [29] for other formulations).

Once the inversion path is selected, we write the cost functional (5) as

$$J(\Omega_i) = \frac{1}{2}\sum_{j=1}^{N} f(t_j) \int_{\Gamma_{\text{meas}}} (U_{\text{total}}(\mathbf{x},t_j) - U_{\text{meas}}(\mathbf{x},t_j))^2 \mathrm{d}l_{\mathbf{x}}$$
$$= \frac{1}{2}\sum_{j=1}^{N} f(t_j) \int_{\Gamma_{\text{meas}}} \left| \int_{-\infty}^{\infty} \mathrm{e}^{t_j\gamma(\theta)} u_{\text{total},\gamma(\theta)}(\mathbf{x}) \frac{\gamma'(\theta)}{2\pi\imath} \mathrm{d}\theta - U_{\text{meas}}(\mathbf{x},t_j) \right|^2 \mathrm{d}l_{\mathbf{x}}. \tag{18}$$

Here, $u_{\text{total},\gamma(\theta)} = u_{\gamma(\theta)} + u_{\text{inc},\gamma(\theta)}$, where $u_{\text{inc},\gamma(\theta)}(\mathbf{x}) = u_{\text{inc}}(\mathbf{x},\gamma(\theta))$ is defined in (15) and $u_{\gamma(\theta)}$ solves (14)–(16) with $s = \gamma(\theta)$. Notice that $U_{\text{total}}(\mathbf{x},t)$ and $U_{\text{meas}}(\mathbf{x},t)$ are real-valued functions. However, for each value of θ, the function $u_{\text{total},\gamma(\theta)}(\mathbf{x})$ as well as the factors $\mathrm{e}^{t_j\gamma(\theta)}$ and $\gamma'(\theta)$ are complex-valued.

3.3. Numerical scheme

The idea now is to discretize integrals from $-\infty$ to ∞ by means of a truncated trapezoidal rule. The inversion formula (17) is approximated by

$$U(\mathbf{x},t) \sim \sum_{\ell=-m}^{m} c_\ell \mathrm{e}^{ts_\ell} u(\mathbf{x},s_\ell) \tag{19}$$

with nodes and weights

$$s_\ell := \gamma\left(\frac{\log(m)}{m}\ell\right), \quad c_\ell := \frac{\log(m)}{2\pi\imath m}\gamma'\left(\frac{\log(m)}{m}\ell\right)$$

and where $u(\mathbf{x},s_\ell) = u_{s_\ell}(\mathbf{x})$ solves problem (14)–(16) with $s = s_\ell$. Few nodes are needed for a good approximation, since convergence is exponential in m. Convergence and error studies depending on m are found in [19]. For the problems we are dealing with, the values $5 \leqslant m \leqslant 10$ provide relative errors of order 10^{-4}. Therefore, only a few stationary problems have to be solved in order to obtain a good approximation. Furthermore, by the symmetry of the selected path and the problems involved, only $m+1$ stationary problems have to be solved, because $u(\cdot,\overline{s_\ell})$ is computed using $u(\cdot,s_\ell)$. Moreover, once m has been fixed and $u_{s_\ell}(\mathbf{x})$ computed, formula (19) holds for any t in the observed time interval with the same accuracy.

The cost functional (18) is approximated by

$$J(\Omega_i) := \frac{1}{2}\sum_{j=1}^{N} f(t_j) \int_{\Gamma_{\text{meas}}} \left| \sum_{\ell=-m}^{m} c_\ell \mathrm{e}^{t_j s_\ell} u_{\text{total},s_\ell}(\mathbf{x}) - U_{\text{meas}}(\mathbf{x},t_j) \right|^2 \mathrm{d}l_{\mathbf{x}}. \tag{20}$$

Here, $u_{\text{total},s_\ell} = u_{\text{inc},s_\ell} + u_{s_\ell}$, where $u_{\text{inc},s_\ell}(\mathbf{x}) = u_{\text{inc}}(\mathbf{x},s_\ell)$ is defined in (15) and u_{s_ℓ} solves (14)–(16) with $s = s_\ell$. Our approximate optimization problem has now $2m+1$ restrictions of the form (14)–(16). As said before, only $m+1$ forward stationary problems must be solved by symmetry.

The following result is proven in Appendix A.

Theorem 3.2. *The topological derivative of the cost functional (20) in $\mathbb{R}^n \setminus \overline{\Omega}_i$, $n = 2$ or 3, is given by*

$$D_T(\mathbf{x}, \mathbb{R}^n \setminus \overline{\Omega}_i) = \mathrm{Re}\left[\sum_{\ell=-m}^{m} \left(\frac{n(1-\alpha_i)}{n-1+\alpha_i} \nabla u_{\text{total},s_\ell}(\mathbf{x}) \nabla p_{s_\ell}(\mathbf{x}) + \frac{(\kappa_i - \kappa_e)s_\ell}{\kappa_e \kappa_i} u_{\text{total},s_\ell}(\mathbf{x}) p_{s_\ell}(\mathbf{x}) \right) \right], \tag{21}$$

where the continuous function p_{s_ℓ} solves

$$\begin{cases} \Delta p + \lambda_{s_\ell,e}^2 p = B_\ell \delta_{\Gamma_{\text{meas}}} & \text{in } \Omega_e, \\ \alpha_i \Delta p + \lambda_{s_\ell,i}^2 p = 0 & \text{in } \Omega_i, \\ p^- - p^+ = 0 & \text{on } \Gamma, \\ \alpha_i \partial_{\mathbf{n}} p^- - \partial_{\mathbf{n}} p^+ = 0 & \text{on } \Gamma, \\ \lim\limits_{r\to\infty} r^{(n-1)/2}(\partial_r p - \imath\lambda_{s_\ell,e} p) = 0 \end{cases} \tag{22}$$

with

$$B_\ell(\mathbf{x}) := \sum_{j=1}^{N} f(t_j) c_\ell \mathrm{e}^{t_j s_\ell} \left(\overline{U_{\mathrm{meas}}(\mathbf{x}, t_j) - \sum_{k=-m}^{m} c_k \mathrm{e}^{t_j s_k} u_{\mathrm{total},s_k}(\mathbf{x})} \right).$$

In this formula, $\frac{(\kappa_i - \kappa_e)s_\ell}{\kappa_e \kappa_i} = \lambda_{s_\ell,i}^2 - \lambda_{s_\ell,e}^2$ replaces the factor appearing in Theorem 3.1 for the time-harmonic-case.

The basic reconstruction scheme sets $\Omega_i = \emptyset$ and computes $D_T(\mathbf{x}, \mathbb{R}^n)$ over a grid of points. The total field is known explicitly: $u_{\mathrm{total},s_\ell} = u_{\mathrm{inc},s_\ell}$ given by (15). In practice, Γ_{meas} is composed of sampling points $\mathbf{x}_1, \ldots, \mathbf{x}_M$ and the solution to the adjoint problem (22) is given by

$$p_{s_\ell}(\mathbf{x}) = -\sum_{k=1}^{M} \phi_{\lambda_{s_\ell,e}}(\mathbf{x}, \mathbf{x}_k) B_\ell(\mathbf{x}_k), \tag{23}$$

where $\phi_{\lambda_{s_\ell,e}}$ is the fundamental solution of $\Delta u + \lambda_{s_\ell,e}^2 u = 0$ defined in (3). Scatterers are likely to be located in the regions where $D_T(\mathbf{x}, \mathbb{R}^n)$ takes large negative values.

The resulting scheme is cheap, because the adjoint and forward fields are known explicitly. Also, the cost of adding new information coming from measurements at other times (in a fixed time interval) or detector locations is negligible. The range for m is fixed and the required forward fields have already been computed. One has just to update p_{s_ℓ} by adding to B_ℓ the contribution of the new time or by adding to p_{s_ℓ} the contribution of the new receptor.

3.4. Iterative schemes

The basic scheme proposed in Section 3.3 is able to locate the scatterers at low cost, at least when they have similar sizes and are placed at a certain distance. If we need a precise reconstruction of their shape, we may resort to iterative schemes.

For a detailed description of iterative schemes in the time-harmonic case we refer to [7,8]. Let us sketch the procedure here. To improve the reconstruction, we select as first guess the domain

$$\Omega_1 := \{\mathbf{x} \in \mathbb{R}^n | D_T(\mathbf{x}, \mathbb{R}^n) \leqslant -C_0\},$$

where C_0 is a certain large positive threshold. Taking now $\mathcal{R} = \mathbb{R}^n \setminus \overline{\Omega}_1$, we compute $D_T(\mathbf{x}, \mathbb{R}^n \setminus \overline{\Omega}_1)$ using formula (21). Iterating this procedure, we generate a nested sequence of scatterers

$$\Omega_{k+1} = \Omega_k \cup \{\mathbf{x} \in \mathbb{R}^n \setminus \overline{\Omega}_k | D_T(\mathbf{x}, \mathbb{R}^n \setminus \overline{\Omega}_k) \leqslant -C_k\},$$

where C_k is a decreasing sequence of positive numbers.

The cost of computing topological derivatives in the successive iterations increases because $\Omega_i = \Omega_k \neq \emptyset$, the forward and adjoint fields are not known analytically and must be calculated numerically. In our two-dimensional examples presented in Section 4, this is done using a boundary integral formulation proposed in [28]. The space discretization is carried out by considering a fully discrete version of a Galerkin method using the space of trigonometric polynomials. The resulting scheme has superalgebraic order of convergence with respect to the discretization parameter if the boundary Γ is infinitely smooth, as it happens in our examples. We refer to [28] and references therein for further details.

The above iterative scheme usually captures scatterers of different sizes provided the boundary of each scatterer has one component. To recover obstacles with more complex shapes (annular shapes, for instance) a refined strategy is needed. An alternative iterative scheme allows to add or remove points from an approximate scatterer at any stage using an extended notion of topological derivative [7]. The idea is to use formula (7) for $\mathbf{x} \in \mathcal{R} = \mathbb{R}^n \setminus \overline{\Omega}_k$ and extend it to $\mathbf{x} \in \Omega_k$, removing $B_\varepsilon(\mathbf{x})$ from Ω_k when computing the functionals. In this way, the topological derivative is defined for all $\mathbf{x} \in \mathbb{R}^n$ and we may implement a different iteration

$$\Omega_{k+1} = \{\mathbf{x} \in \mathbb{R}^n | D_T(\mathbf{x}, \mathbb{R}^n \setminus \overline{\Omega}_k) \leqslant -C_k\}.$$

4. Reconstruction tests

In this section, we present numerical experiments comparing reconstructions of inclusions using time-harmonic and delta pulse excitations in a problem set in the half plane $\mathbb{R}^2_-$. In both cases, incident waves are originated at sources located on the upper boundary $\Pi := \{(x,0),\ x \in \mathbb{R}\}$. The temperature is measured at a set of sampling points located on Π.

Either for time-harmonic incident waves or delta-pulse excitations, the computation of the topological derivatives (11) and (21) is rather cheap. We just have to evaluate a few known functions at a grid of points. In the time-harmonic case, u_{inc} is given by (2) and (3) and p by (13). For the time-dependent problem, the functions u_{inc,s_ℓ} are given by (15) and the adjoint states p_{s_ℓ} are computed by formula (23).

We select an obstacle Ω_i with physical parameters $\kappa_i = 1/4$ and $\alpha_i = 1$. The conductivity of the exterior matrix $\Omega_e = \mathbb{R}^2_- \setminus \overline{\Omega}_i$ is $\kappa_e = 4$. The interface separating both materials is parameterized as

$$\mathbf{x} : \mathbb{R} \to \Gamma, \quad \mathbf{x}(s) := (r(s)\cos(s), \quad -1.2 + r(s)\sin(s)),$$

where

$$r(s) := 0.5 + 0.05(\sin(2s + \pi/4) - \sin(3s)).$$

Notice that the solution of the forward problem for the true obstacle Ω_i agrees with the measured data at the detector locations. Typically, the values of U_{meas} at the detector locations are measured experimentally. In our tests, the measured data U_{meas} are generated by solving the corresponding forward problem and adding a small relative noise about 0.1%.

Let us first discuss a time-harmonic test. As said before, thermal waves have a short range of action. The size of the region influenced by the incident wave depends on the frequency. At high frequencies, penetration is weak. By lowering the frequency we increase the distance traveled by the wave.

In Fig. 2, we represent the topological derivative (11) for different values of the frequency ω. Recall that the wave-numbers in the Helmholtz transmission problem and the frequency of the incident radiation are related by the identities

$$\lambda_\ell = (1+\imath)\sqrt{\omega/(2\kappa_\ell)}, \quad \ell = e, i.$$

We have considered incident waves generated at 24 uniformly distributed source points on Π. Measurements were taken on 25 sampling points that form a staggered grid with respect to the source points, see Fig. 2. Neither low, nor high frequencies provide accurate information about the size and the shape of the obstacle. We can only infer its approximate location, although not the correct depth. As expected, the topological derivative tries to capture the part of the obstacle that is closer to Π (the 'illuminated' part). This behavior is not surprising, since we are just considering incident waves generated at sources located on Π and measuring the temperature at receptors located at the same boundary. No information from other directions is available. As pointed out in [7,13,15] for acoustic and elastic scattering, restricted distributions of source points (or limited incidence angles in case of planar incident waves) result in the appearance of 'shadow' and 'illuminated' regions. The topological derivative tends to be useful only on the 'illuminated' region. This effect is amplified here by the strong damping of thermal waves, which makes them very sensitive to the presence of defects located near the surface, but not to the ones that are far from it.

Let us repeat the experiment considering incident fields of the form (4) with source points located on Π. We compute the topological derivative of the approximate cost functional (20) with $f = 1$ and $N = 1$, for different times t_1. The results are shown in Fig. 3 considering the same source and sampling points as in the time-harmonic case.

For small values of t, the illuminated region is reconstructed with more precision than the shadow parts. For the intermediate values of t, there is not a big difference between these two regions. As t increases, one can even recover more information about the shadow region than about the illuminated one. Higher values of t give almost no information about any of the regions. For an intermediate range of times, the size and location of the obstacle are reasonably predicted, as shown in Fig. 3(c)–(e).

In the tests represented in Figs. 2 and 3, we had at our disposal data at 25 sampling points for 24 incident fields. This amounts 600 data. Increasing the number of sampling points and/or incident fields does not result in significant improvements.

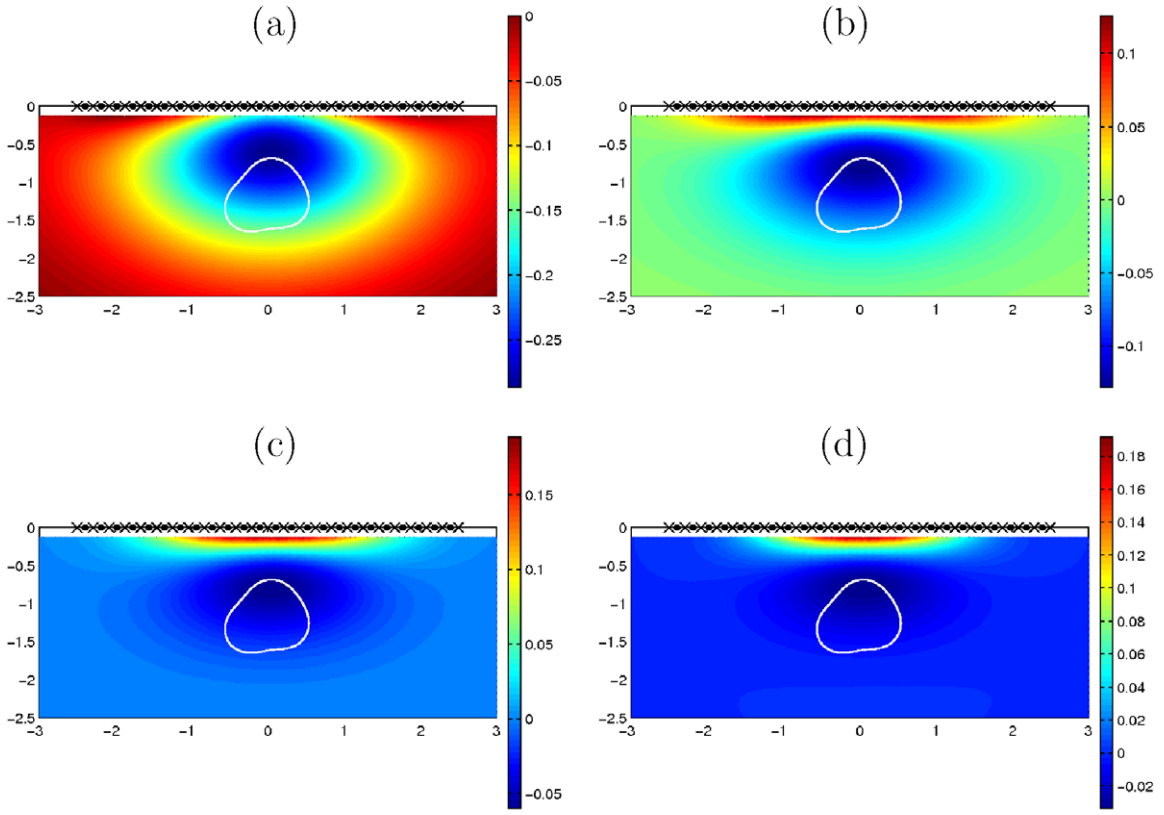

Fig. 2. Topological derivative with data from 24 incident sources ('•') at 25 sampling points ('×') for different frequencies: (a) $\omega = 2$, (b) $\omega = 4$, (c) $\omega = 7$, (d) $\omega = 10$.

We have carried out a number of numerical experiments for different geometries, sizes and depths. They seem to indicate that, depending on the size and depth of the obstacles, a suitable choice of the time at which measurements are taken allows for quite accurate reconstructions. For our incident fields, the time interval is defined by the times at which the expanding gaussians reach and pass the obstacles. For a fixed geometrical configuration, the optimal values of the observation times depend on the physical parameters, that is, on the values of κ_e, κ_i and α_i. In general, for each physical and geometrical configuration there exists a time interval that produces much more reliable reconstructions than simple time-harmonic excitations.

In practice, we know the values of κ_e, κ_i and α_i but we do not have information about the size and/or depth of the obstacles. Hence, we do not know how to choose the correct value of t to obtain an optimal reconstruction. This difficulty is overcome by considering cost functionals of the form (20) with $N > 1$, in which measurements are taken at different times. We compare the information provided by the topological derivative (21) for the following weight functions:

$$f_1(t) = \max_{\mathbf{x}\in\{\mathbf{x}_1,\ldots,\mathbf{x}_M\}} |U_{\text{meas}}(\mathbf{x},t)|^{-1}, \tag{24}$$

$$f_2(t) = \max_{\mathbf{x}\in\{\mathbf{x}_1,\ldots,\mathbf{x}_M\}} |U_{\text{inc}}(\mathbf{x},t)|^{-1}, \tag{25}$$

$$f_3(t) = \max_{\mathbf{x}\in\{\mathbf{x}_1,\ldots,\mathbf{x}_M\}} |U_{\text{meas}}(\mathbf{x},t)|^{-2}, \tag{26}$$

$$f_4(t) = \max_{\mathbf{x}\in\{\mathbf{x}_1,\ldots,\mathbf{x}_M\}} |U_{\text{inc}}(\mathbf{x},t)|^{-2}, \tag{27}$$

and the sequence of times $t_1 = 0.2$, $t_2 = 0.25$, $t_3 = 0.3$, $t_4 = 0.35$, $t_5 = 0.4$, $t_6 = 0.45$, keeping the same source and sampling points as in the previous tests. This is equivalent to averaging in different ways the topological

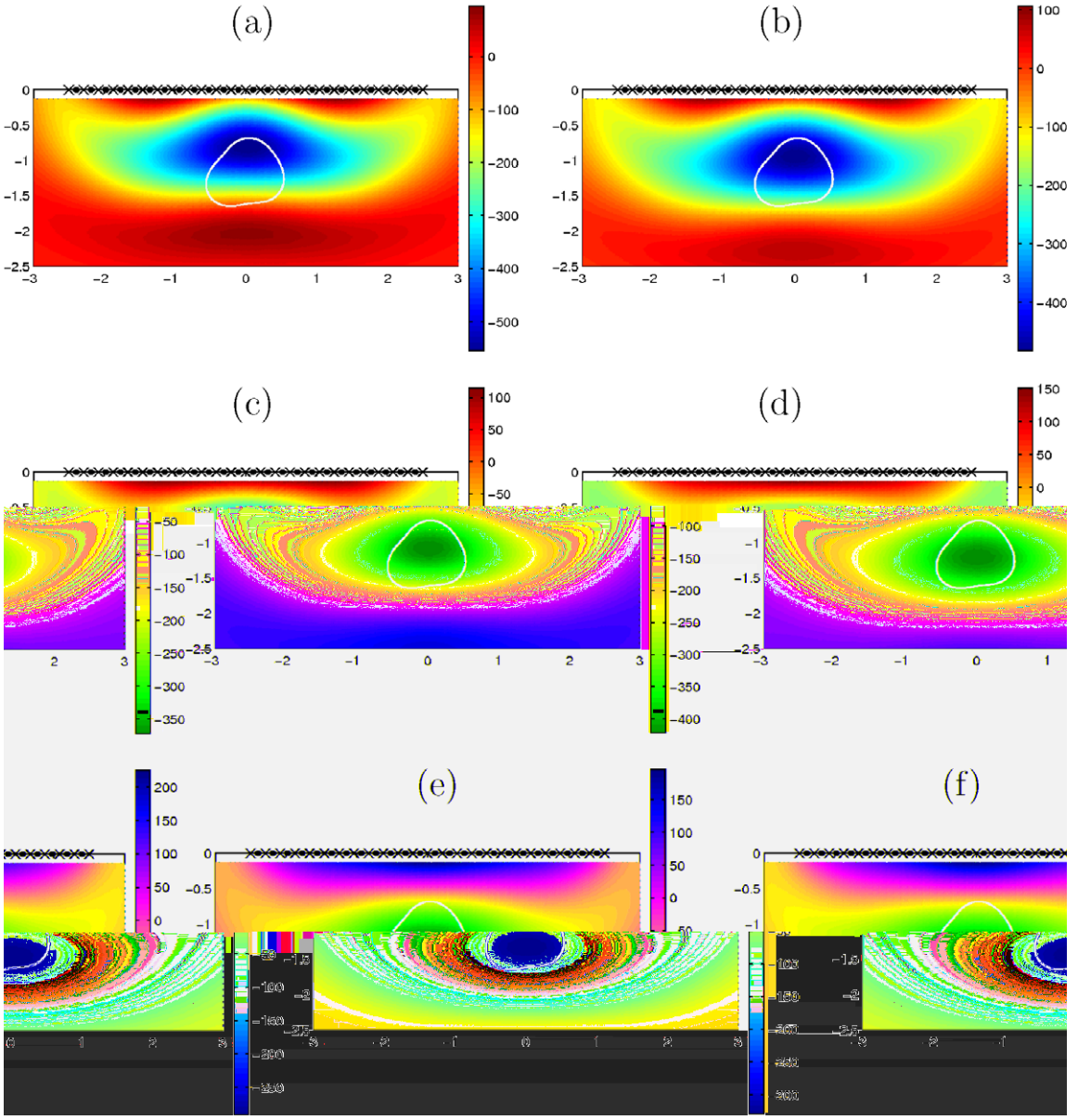

Fig. 3. Topological derivative with data from 24 incident sources ('•') at 25 sampling points ('×') at different times: (a) $t_1 = 0.2$, (b) $t_1 = 0.25$, (c) $t_1 = 0.3$, (d) $t_1 = 0.35$, (e) $t_1 = 0.4$, (f) $t_1 = 0.45$.

derivatives plotted in Fig. 3. The results are shown in Fig. 4. We observe that the overall reconstruction quality in the four cases is quite good, f_4 being possibly the function that provides the best predictions. For each plot in Fig. 4 we have used $600 \times 6 = 3600$ data.

The fact that one can obtain reliable reconstructions by measuring the temperature over a carefully chosen time interval was already noticed in [18] for reconstructions of corrosion functions in given geometries. In that work, it is also observed that delta-pulse excitations provide the same quality of reconstruction for shadow and illuminated regions.

We explore now the performance of the method when increasing the number of observation times while decreasing the number of sampling and source points. In Fig. 5, we represent the topological derivative of the cost functional (20) for the weight function f_4 defined in (27). The total amount of data for each example

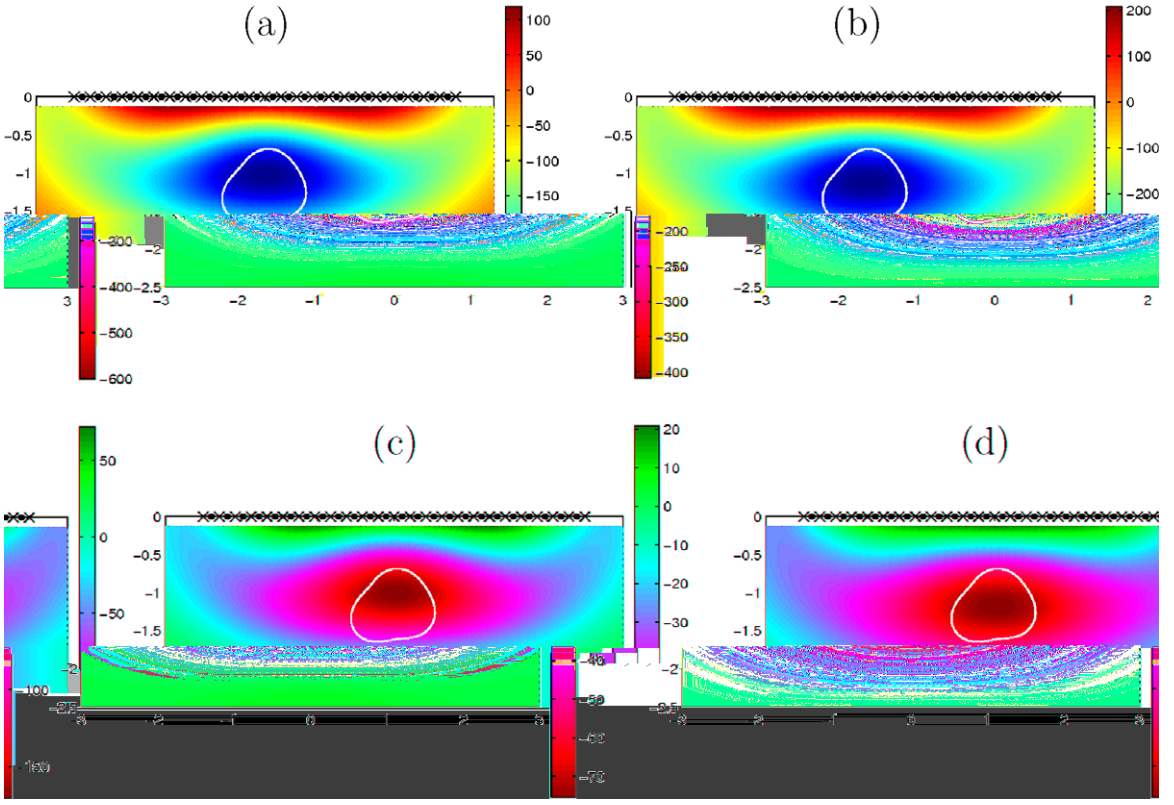

Fig. 4. Topological derivative of the cost functional (20) for the weight functions defined in (24)–(27) with data from 24 incident sources ('•') at 25 sampling points ('×') at times $t_1, \ldots, t_6 = 0.2, 0.25, 0.3, 0.35, 0.4, 0.45$: (a) $f = f_1$, (b) $f = f_2$, (c) $f = f_3$, (d) $f = f_4$.

in Fig. 5 is 360. These examples illustrate that a small number of observation points or incident fields allow for reasonable reconstructions if we measure the temperature many times.

Let us consider now the geometry with two objects in Fig. 6. Our method clearly identifies two objects, their correct depth and approximate sizes. When the objects have different sizes and/or are very closed to each other, this scheme could fail in obtaining the correct number of objects or their location.

First guesses obtained by computing topological derivatives in the whole space can be further improved by the iterative method described in Section 3.4. Shapes can be reconstructed with precision and the correct number of obstacles (in case they have different sizes or are very close) is found. Fig. 7(a) depicts the topological derivative of the cost functional (20) with weight function f_4 when the temperature is measured at the seven receptors ('×') and fifteen observation times in $[0.2, 0.45]$ for six source points ('•'). We detect the presence of a single object, its approximate size and location, but we cannot predict its shape. In Fig. 7(b), we show the first guess Ω_1, superimposed on the topological derivative $D_T(\mathbf{x}, \mathbb{R}^2_- \setminus \overline{\Omega}_1)$. The subsequent plots illustrate the improvement in a few iterations. In five steps the shape, size and location of the object are almost determined.

In Fig. 8, the same iterative procedure is applied to a geometry with two objets. A first guess Ω_1 is obtained using the values of the topological derivative represented in Fig. 6. Again, after a few iterations both objects are satisfactorily reconstructed, specially the regions which are closer to the detector locations Γ_{meas}.

5. Topological derivatives for the time-dependent problem: Direct approach

Let us compare the computational approach we have developed with strategies based on computing the topological derivative of the original time-dependent functional. Below, we give an expression for this derivative when $n = 2$.

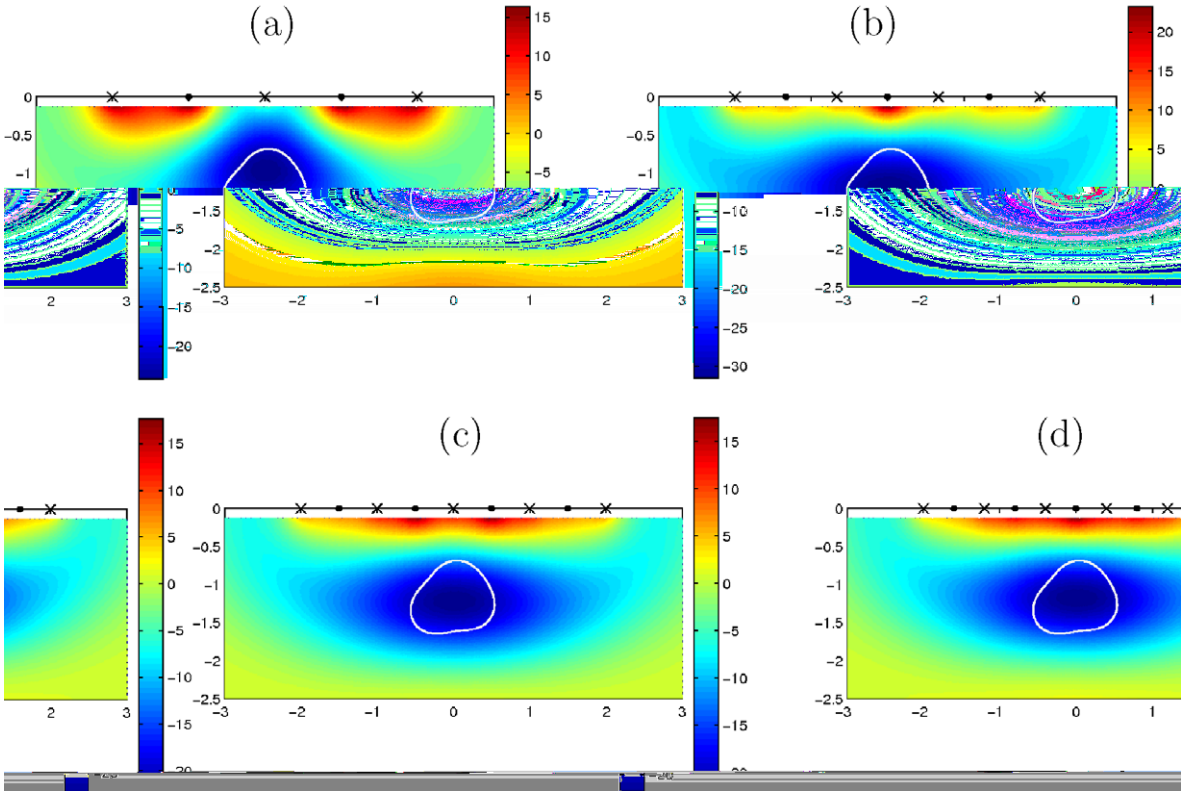

Fig. 5. Topological derivative of the cost functional (20) with weight function f_4: (a) 2 source points ('•'), 3 observation points ('×'), $N = 60$ for times in $[0.2, 0.45]$; (b) 3 source points ('•'), 4 observation points ('×'), $N = 30$ for times in $[0.2, 0.45]$; (c) 4 source points ('•'), 5 observation points ('×'), $N = 18$ for times in $[0.2, 0.45]$; (d) 5 source points ('•'), 6 observation points ('×'), $N = 12$ for times in $[0.2,\ 0.45]$.

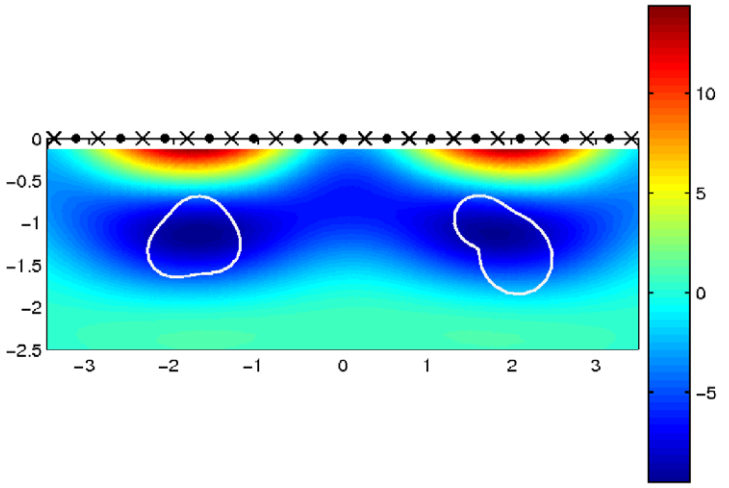

Fig. 6. Topological derivative of the cost functional (20) with weight function f_4.

Theorem 5.1. *For the incident fields U_{inc} defined in (4), the topological derivative of the functional (5) is*

$$D_T(\mathbf{x}, \mathbb{R}^2) = \int_0^T \left[\frac{2(1-\alpha_i)}{1+\alpha_i} \nabla U_{\text{total}}(\mathbf{x}, t) \nabla P(\mathbf{x}, t) + \left(-\frac{1}{\kappa_i} + \frac{1}{\kappa_e} \right) U_{\text{total},t}(\mathbf{x}, t) P(\mathbf{x}, t) \right] \mathrm{d}t, \tag{28}$$

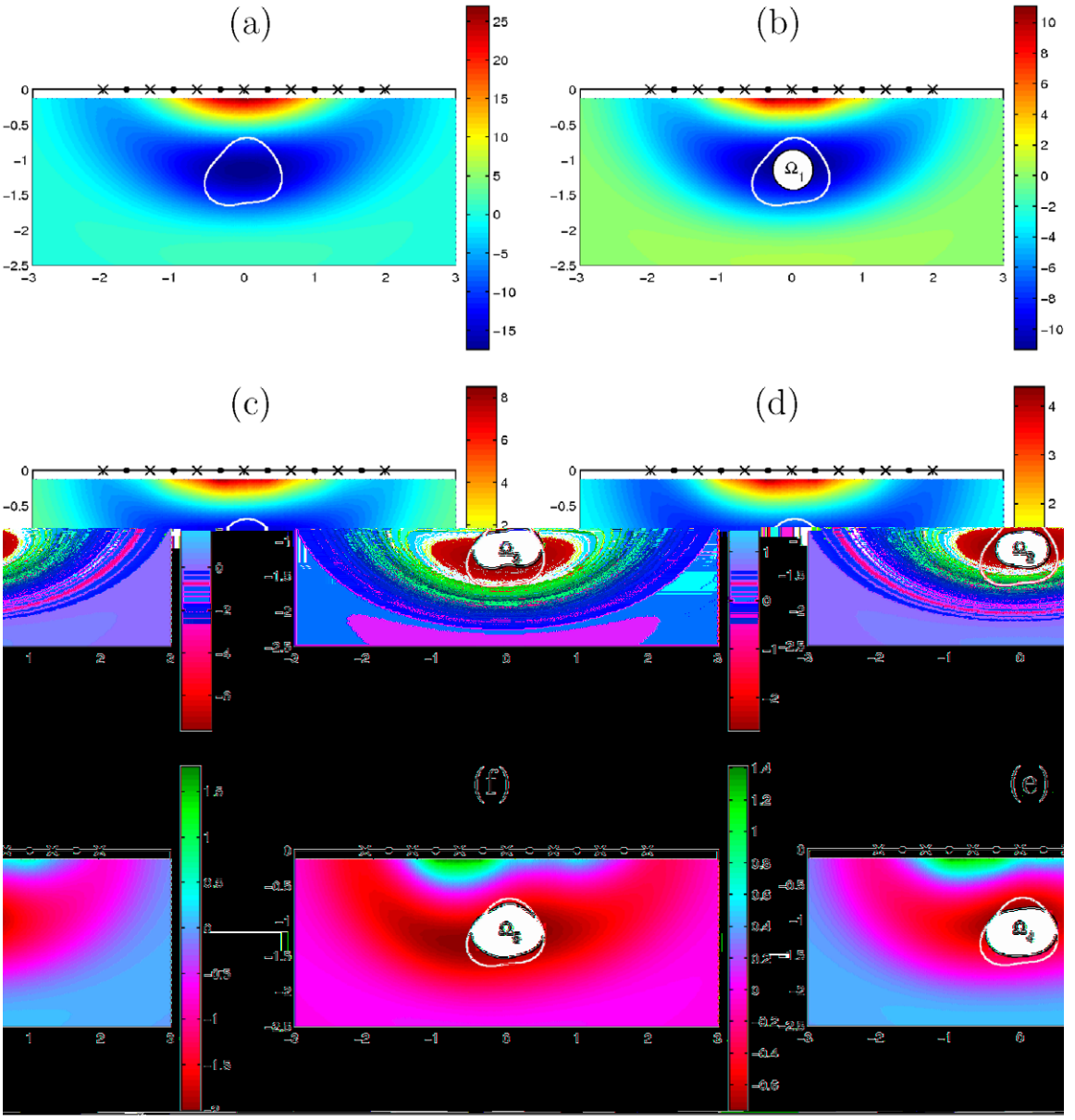

Fig. 7. First iterations of the hybrid method.

when $\mathbf{x} \in \mathbb{R}^2$, $\mathbf{x} \neq \mathbf{x}_0$, *and* $\mathbf{x} \neq \mathbf{x}_k$, $k = 1, \ldots, M$, $\{\mathbf{x}_1, \ldots, \mathbf{x}_M\}$ *being the set of sampling points on* Γ_{meas}. *The forward and adjoint fields are known*: $U_{\text{total}} = U_{\text{inc}}$ *and*

$$P(\mathbf{x}, t) = \sum_{k=1}^{M} \sum_{j|t \leqslant t_j \leqslant T} G_{\kappa_e}(\mathbf{x} - \mathbf{x}_k, t_j - t) B(\mathbf{x}_k, t_j), \tag{29}$$

where

$$B(\mathbf{x}, t) = f(t)(U_{\text{total}}(\mathbf{x}, t) - U_{\text{meas}}(\mathbf{x}, t)) \tag{30}$$

and G_{κ_e} *is the two-dimensional heat kernel for the exterior problem. When* $\mathbb{R}^2$ *is replaced by* $\mathbb{R}^2 \setminus \overline{\Omega}$ *the topological derivative is again given by* (28), *with forward and adjoint fields solving transmission problems for the heat equation with* $\Omega_i = \Omega$.

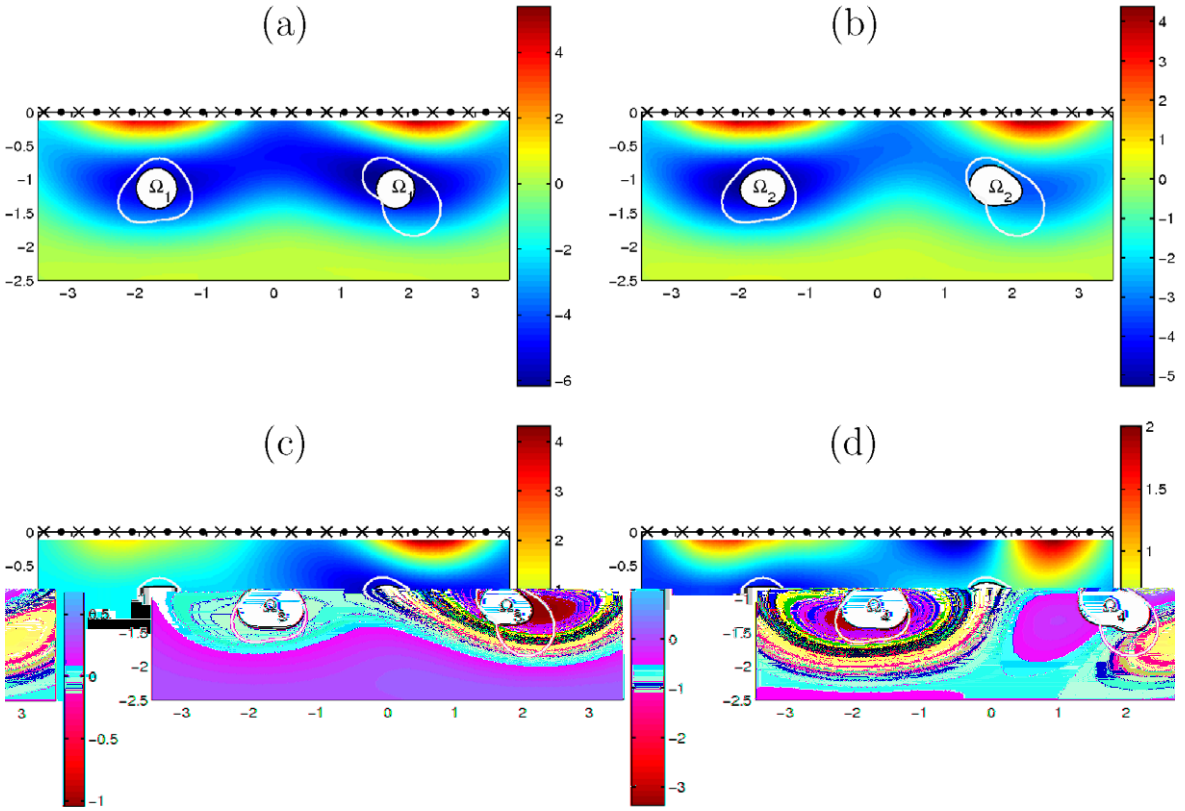

Fig. 8. First iterations of the hybrid method.

The proof is given in Appendix B. In (28), we may replace U_tP by $-UP_t$ because $U(\mathbf{x},0) = P(\mathbf{x},T) = 0$ when $\mathbf{x}$ is not a source point. However, the integrand U_tP behaves better from a numerical point of view. In spite of the singularities of U at $t = 0$ and P at t_j, the integrals are finite because the exponentials cancel out the singularity when $\mathbf{x}$ is not a source or a sampling point.

The asymmetric role played by variables t and $\mathbf{x}$ observed in (28) is due to the fact that we look for spatial domains Ω and the topological derivative is computed using balls $B_\varepsilon(\mathbf{x})$ in space.

Unlike formula (21) for $\Omega_i = \emptyset$, formula (28) is not fully explicit due to the time integral. Our tests with $\alpha_i = 1$ and U_{inc} defined in (4), indicate that the objects are indistinguishable unless T is chosen properly and an adequate quadrature formula with the right number of nodes, distributed in the right way and with right weights is employed. For each geometrical configuration, a reasonable choice depends on the sources, sampling points and times. There is not a clear recipe to select T. The particular integrands we are working with make the result of the numerical integration very sensitive to the quadrature formula. Is seems that nodes must be distributed far enough from the times t_j and 0. We have managed to fit the parameters in the quadrature formula for known obstacle geometries. In practice, the geometry is unknown and it is unlikely that the quadrature formula we use will be fitted to the problem.

Hybrid schemes combining time recording with topological derivative based iterative schemes relying in (28) are more expensive than those relying on Laplace transforms due to the cost of evaluating the integral in (28) and computing the adjoint and forward fields if Laplace transforms are avoided. At each iteration, we must solve two transmission problems for the heat equation in unbounded domains with an inclusion of changing shape. The infinite spatial domain has to be truncated to a large domain without affecting the solutions. The heat equations can be discretized using finite elements but the mesh changes at each iteration as Ω_i changes. The forward and adjoint fields may then be approximated solving large systems of ordinary differential equations. Computing at each time step the right-hand side for many time steps makes this

approach much expensive than solving a few boundary integral equations with the Laplace approach. In fact, the combination of Laplace transforms with boundary integral techniques allows to implement fast parallelizable solvers to evaluate the solutions of these transmission problems at certain times (without computing the solutions for previous times).

6. Conclusions

We have extended topological derivative techniques to a time-dependent setting, considering in particular shape reconstruction problems by thermal measurements in a semi-infinite medium. The time-dependent problem is transformed in a family of stationary problems by means of Laplace transforms. Selecting an adequate path for the inversion formula, the original time-dependent fields can be accurately approximated by a quadrature rule involving few points. The shape reconstruction problem is then approximated by a constrained optimization problem for a functional defined in terms of the discretized numerical inversion formula. The constraints are a finite set of stationary Helmholtz transmission problems with complex wave-numbers. Explicit expressions for the topological derivative of this functional in terms of forward and adjoint fields are given.

By computing the topological derivative of the functional in the whole space, we find good guesses of the number and location of obstacles at low cost. The adjoint and forward fields are known explicitly. Numerical experiments show that thermal measurements allow for reasonable reconstructions of objects when they are placed near the surface and measurements are made on that surface during a well chosen time interval. A small number of sampling points or incident fields allow for good reconstructions if we measure the temperature many times. For the selected time-dependent incident fields, we obtain precise information on both the illuminated and shadow parts of the objects.

We have shown that scattering by time-harmonic incident fields produce worse results, specially in the shadow parts. In this case, we might improve the reconstruction by resorting to the iterative schemes developed in [7] or by successively deforming the contours using level-set methods [5,11]. This requires solving a large number of forward and adjoint problems in variable exterior domains. Using general time-dependent sources, we avoid solving these auxiliary spatial problems by averaging information at different times using explicit formulae for the adjoint and forward fields. Thus, the computational cost is smaller and the codes are easy to parallelize.

Hybrid schemes combining time recording with topological derivative based iterative methods have been tested. They sharpen the description of the shapes provided by the basic time averaging scheme, at a higher cost. In each iteration the forward and adjoint fields have to be computed by boundary integral techniques. The usage of general time-dependent sources and time averaging reduces the number of iterations required for a precise description of sizes and shapes, even for a few sources and a few observation points.

Although we have focused on diffusion problems with transmission boundary conditions at the interface between the inclusions and the surrounding matrix, the ideas can easily be adapted to acoustic problems and other boundary conditions: Dirichlet, Neumann, mixed, Engquist–Nédélec, etc. The numerical tests presented in this paper are restricted to two-dimensional geometries to reduce the computational cost. Alternative schemes based on computing the topological derivative of the time-dependent functional are not competitive at the present time.

Our techniques may be useful in other contexts in which data are recorded during a certain time, such as biomedical applications [9] or synthetic aperture radar [4].

Acknowledgments

This research has been supported by MEC/FEDER Projects MAT2005-05730-C02-02 and MTM2007-63204, and by PR27/05-13939, CM-910143.

Appendix A. Derivation of the topological derivative for the Laplace-transformed problem

In this appendix, we prove Theorem 3.2. The formal proof follows the same steps as the proof of Theorem 3.1 for the time-harmonic case, see [8] and references therein for details. By linearity, we can consider indepen-

dently each value $t = t_j$, that is, we decompose the functional (20) as $J(\Omega_i) = \sum_{j=1}^{N} f(t_j) J_j(\Omega_i)$ and compute the topological derivative of each $J_j(\Omega_i)$. Then, we add the different contributions to get the final formula:

Step 1: Variational formulation. Recall that u_{s_ℓ} solves the transmission problem (14)–(16). Then, the total field $u_\ell = u_{\text{total},s_\ell}$ (equal to u_{s_ℓ} inside Ω_i and $u_{s_\ell} + u_{\text{inc},s_\ell}$ outside) solves the following variational problem: Find $u_\ell \in H^1(B_R)$ such that

$$b_\ell(\Omega_i; u_\ell, v) = l_\ell(\Omega_i; v) \quad \forall v \in H^1(B_R), \tag{A.1}$$

where

$$b_\ell(\Omega_i; u, v) := \int_{\Omega_e \cap B_R} (\nabla u \nabla \bar{v} - \lambda_{s_\ell,e}^2 u\bar{v}) \mathrm{d}\mathbf{z} + \int_{\Omega_i} (\alpha_i \nabla u \nabla \bar{v} - \lambda_{s_\ell,i}^2 u\bar{v}) \mathrm{d}\mathbf{z} - \int_{\Gamma_R} Lu\bar{v}\, \mathrm{d}l,$$

$$l_\ell(v) := \int_{\Gamma_R} (\partial_{\mathbf{n}} u_{\text{inc},s_\ell} - L u_{\text{inc},s_\ell})\bar{v}\, \mathrm{d}l.$$

Here, $B_R = B(0,R)$ is a large ball containing Ω_i, $\Gamma_R = \partial B_R$ and L is the Dirichlet-to-Neumann operator on Γ_R. This operator associates to any Dirichlet data on Γ_R the normal derivative on Γ_R of the outgoing solution to the exterior problem set in $\mathbb{R}^n \setminus \overline{B_R}$.

Step 2: Transformed functional. We introduce a family of deformations $\phi_\tau(\mathbf{z}) = \mathbf{z} + \tau \mathbf{V}(\mathbf{z})$ along a vector field $\mathbf{V}$ which decreases rapidly to zero away from Γ and $\mathbf{V}(\mathbf{z}) = V_n \mathbf{n}(\mathbf{z})$ if $\mathbf{z} \in \Gamma$, V_n being a negative constant. Thus, $\phi_\tau(\Gamma_{\text{meas}}) = \Gamma_{\text{meas}}$. Let us set $\Omega_{i,\tau} := \phi_\tau(\Omega_i)$ and $\Omega_{e,\tau} := \phi_\tau(\Omega_e) = \mathbb{R}^n \setminus \overline{\Omega}_{i,\tau}$. The transformed functionals $J_j(\Omega_{i,\tau})$ are given by

$$J_j(\Omega_{i,\tau}) := \frac{1}{2} \int_{\Gamma_{\text{meas}}} \left| \sum_{\ell=-m}^{m} \mathrm{e}^{t_j s_\ell} c_\ell u_{\ell,\tau}(\mathbf{x}) - U_{\text{meas}}(\mathbf{x}, t_j) \right|^2 \mathrm{d}l_{\mathbf{x}}, \tag{A.2}$$

where $u_{\ell,\tau}$ solves the variational problem in the transformed domains: Find $u_{\ell,\tau} \in H^1(B_R)$ such that $b_\ell(\Omega_{i,\tau}; u_{\ell,\tau}, v) = l_\ell(v)$, $\forall v \in H^1(B_R)$.

Step 3: Adjoint field. The derivative of the transformed functional with respect to the deformation parameter τ is

$$\begin{aligned} \frac{\mathrm{d}}{\mathrm{d}\tau} J_j(\Omega_{i,\tau})\Big|_{\tau=0} &= \mathrm{Re}\left[\int_{\Gamma_{\text{meas}}} \left(\overline{(\widehat{U}_{\text{total}}(\mathbf{x}, t_j) - U_{\text{meas}}(\mathbf{x}, t_j))} \sum_{\ell=-m}^{m} \mathrm{e}^{t_j s_\ell} c_\ell \dot{u}_\ell(\mathbf{x}) \right) \mathrm{d}l_{\mathbf{x}} \right] \\ &= \mathrm{Re}\left[\sum_{\ell=-m}^{m} \left(\int_{\Gamma_{\text{meas}}} \overline{(\widehat{U}_{\text{total}}(\mathbf{x}, t_j) - U_{\text{meas}}(\mathbf{x}, t_j))} \dot{u}_\ell(\mathbf{x}) \mathrm{d}l_{\mathbf{x}} \right) \mathrm{e}^{t_j s_\ell} c_\ell \right] \end{aligned}$$

where $\dot{u}_\ell = \frac{\mathrm{d}}{\mathrm{d}\tau} u_{\ell,\tau}\big|_{\tau=0}$ and $\widehat{U}_{\text{total}}(\mathbf{x}, t_j) = \sum_{\ell=-m}^{m} \mathrm{e}^{t_j s_\ell} c_\ell u_\ell(\mathbf{x})$. To avoid the computation of $\dot{u}_\ell$ we introduce the modified Lagrangian

$$\mathcal{L}_j(\Omega_{i,\tau}; v_\ell, p_\ell) = J_j(\Omega_{i,\tau}) - \mathrm{Re}\left[\sum_{\ell=-m}^{m} \mathrm{e}^{t_j s_\ell} c_\ell (b_\ell(\Omega_{i,\tau}; v_\ell, p_\ell) - l_\ell(p_\ell)) \right]$$

for all $v_\ell, p_\ell \in H^1(B_R)$. When $v_\ell = u_{\ell,\tau}$, we have $\mathcal{L}(\Omega_{i,\tau}; u_{\ell,\tau}, p_\ell) = J_j(\Omega_{i,\tau})$, $\forall p_\ell \in H^1(B_R)$. Then, the shape derivative of J_j in the direction $\mathbf{V}$ is

$$\begin{aligned} DJ_j(\Omega_i) \cdot \mathbf{V} = &-\frac{\mathrm{d}}{\mathrm{d}\tau} \mathrm{Re}\left[\sum_{\ell=-m}^{m} \mathrm{e}^{t_j s_\ell} c_\ell b_\ell(\Omega_{i,\tau}; u_\ell, p_\ell) \right]\Big|_{\tau=0} - \mathrm{Re}\left[\sum_{\ell=-m}^{m} \mathrm{e}^{t_j s_\ell} c_\ell b_\ell(\Omega_i; \dot{u}_\ell, p_\ell) \right] \\ &+ \mathrm{Re}\left[\sum_{\ell=-m}^{m} \left(\int_{\Gamma_{\text{meas}}} \overline{(\widehat{U}_{\text{total}}(\mathbf{x}, t_j) - U_{\text{meas}}(\mathbf{x}, t_j))} \dot{u}_\ell(\mathbf{x}) \mathrm{d}l_{\mathbf{x}} \right) \mathrm{e}^{t_j s_\ell} c_\ell \right] \end{aligned} \tag{A.3}$$

This identity is valid for all $p_\ell \in H^1(B_R)$. If we select now p_ℓ^j satisfying

$$b_\ell(\Omega_i; v, p_\ell^j) = -\int_{\Gamma_{\text{meas}}} \overline{(U_{\text{meas}}(\mathbf{x}, t_j) - \widehat{U}_{\text{total}}(\mathbf{x}, t_j))} v(\mathbf{x}) \mathrm{d}l_{\mathbf{x}} \quad \forall v \in H^1(B_R), \tag{A.4}$$

the shape derivative $DJ_j(\Omega_i)\cdot\mathbf{V}$ is given by the first term in (A.3). It is rather simple to show now that the conjugate $\bar{p}_\ell^j$ of p_ℓ^j solves

$$\begin{cases} \Delta p+\lambda_{s_\ell,e}^2 p=\left(\overline{U_{\text{meas}}(\mathbf{x},t_j)-\widehat{U}_{\text{total}}(\mathbf{x},t_j)}\right)\delta_{\Gamma_{\text{meas}}}(\mathbf{x}) & \text{in } \Omega_e,\\ \alpha_i\Delta p+\lambda_{s_\ell,i}^2 p=0 & \text{in } \Omega_i,\\ p^- - p^+=0 & \text{on } \Gamma,\\ \alpha_i\partial_{\mathbf{n}}p^- - \partial_{\mathbf{n}}p^+=0 & \text{on } \Gamma,\\ \lim\limits_{r\to\infty} r^{(n-1)/2}(\partial_r p-\imath\lambda_{s_\ell,e}p)=0. \end{cases} \tag{A.5}$$

Step 4: Shape derivative. The change of variables from the deformed to the original variables is governed by the identities

$$\nabla_{\mathbf{z}_\tau}U=F_\tau^{-\top}\nabla U,\quad \mathrm{d}\mathbf{z}_\tau=\det F_\tau\,\mathrm{d}\mathbf{z},$$
$$\frac{\mathrm{d}}{\mathrm{d}\tau}F_\tau\Big|_{\tau=0}=\nabla\mathbf{V},\quad \frac{\mathrm{d}}{\mathrm{d}\tau}(\nabla_{\mathbf{z}_\tau}U)\Big|_{\tau=0}=-\nabla\mathbf{V}^\top\nabla U,\quad \frac{\mathrm{d}}{\mathrm{d}\tau}\mathrm{d}\mathbf{z}_\tau\Big|_{\tau=0}=\operatorname{div}\mathbf{V}\,\mathrm{d}\mathbf{z},$$

where $F_\tau:=\nabla\phi_\tau=I+\tau\nabla\mathbf{V}$ is the deformation gradient. Let us compute the first term in (A.3) for our choice of the adjoint field:

$$\begin{aligned}\frac{\mathrm{d}}{\mathrm{d}\tau}[b_\ell(\Omega_{i,\tau};u_\ell,p_\ell^j)]\Big|_{\tau=0}&=\int_{\Omega_e\cap B_R}\left[(\nabla u_\ell\nabla\bar{p}_\ell^j-\lambda_{s_\ell,e}^2u_\ell\bar{p}_\ell^j)\operatorname{div}\mathbf{V}-\big((\nabla\mathbf{V}+\nabla\mathbf{V}^\top)\nabla u_\ell\big)\nabla\bar{p}_\ell^j\right]\mathrm{d}\mathbf{z}\\&\quad+\int_{\Omega_i}\left[(\alpha_i\nabla u_\ell\nabla\bar{p}_\ell^j-\lambda_{s_\ell,i}^2u_\ell\bar{p}_\ell^j)\operatorname{div}\mathbf{V}-\alpha_i\big((\nabla\mathbf{V}+\nabla\mathbf{V}^\top)\nabla u_\ell\big)\nabla\bar{p}_\ell^j\right]\mathrm{d}\mathbf{z}.\end{aligned} \tag{A.6}$$

Integrating by parts, using the equations satisfied by u_ℓ and $\bar{p}_\ell^j$, recalling our choice for the normal vector on Γ, and using the transmission conditions at the interface we find:

$$DJ(\Omega_i)\cdot\mathbf{V}=-\mathrm{Re}\left[\sum_{\ell=-m}^{m}\mathrm{e}^{t_js_\ell}c_\ell\int_\Gamma\left[(\lambda_{s_\ell,i}^2-\lambda_{s_\ell,e}^2)u_\ell\bar{p}_\ell^j+(1-\alpha_i)\partial_{\mathbf{t}}u_\ell^-\partial_{\mathbf{t}}\bar{p}_\ell^{j-}+\alpha_i(1-\alpha_i)\partial_{\mathbf{n}}u_\ell^-\partial_{\mathbf{n}}\bar{p}_\ell^{j-}\right]V_n\mathrm{d}l_{\mathbf{z}}\right]. \tag{A.7}$$

Step 5: Topological derivative in the whole space. Let us first calculate the topological derivative of the cost functional J_j when $\mathcal{R}=\mathbb{R}^n$. We set $\Omega_i=B_\varepsilon(\mathbf{x})$, $B_\varepsilon(\mathbf{x})=B(\mathbf{x},\varepsilon)$. The known relationship between topological and shape derivatives [13]:

$$D_T(\mathbf{x},\mathbb{R}^n)=\lim_{\varepsilon\to0}\frac{1}{\mathcal{V}'(\varepsilon)|V_n|}DJ(B_\varepsilon(\mathbf{x}))\cdot\mathbf{V} \tag{A.8}$$

together with formula (A.7) yield

$$D_T(\mathbf{x},\mathbb{R}^n)=\lim_{\varepsilon\to0}\frac{1}{\mathcal{V}'(\varepsilon)}\mathrm{Re}\left[\sum_{\ell=-m}^{m}\mathrm{e}^{t_js_\ell}c_\ell\int_{\Gamma_\varepsilon}\left[(\lambda_{s_\ell,i}^2-\lambda_{s_\ell,e}^2)u_{\ell,\varepsilon}p_{\ell,\varepsilon}+(1-\alpha_i)\partial_{\mathbf{t}}u_{\ell,\varepsilon}^-\partial_{\mathbf{t}}p_{\ell,\varepsilon}^-+\alpha_i(1-\alpha_i)\partial_{\mathbf{n}}u_{\ell,\varepsilon}^-\partial_{\mathbf{n}}p_{\ell,\varepsilon}^-\right]\mathrm{d}l_{\mathbf{z}}\right]. \tag{A.9}$$

Recall that V_n is constant and negative. Here, $u_{\ell,\varepsilon}$ and $p_{\ell,\varepsilon}$ solve (A.1) and (A.5) when $\Omega_i=B_\varepsilon(\mathbf{x})$ and $\Gamma=\Gamma_\varepsilon=\partial B_\varepsilon(\mathbf{x})$. A value for this limit is computed performing an asymptotic expansion of these solutions and their gradients at Γ_ε as in [8]. Let us set

$$u_{\ell,\varepsilon}(\mathbf{z})=u_\ell(\mathbf{z})\chi_{\mathbb{R}^n\setminus\overline{B}_\varepsilon}(\mathbf{z})+v_{\ell,\varepsilon}(\mathbf{z}),\quad p_{\ell,\varepsilon}(\mathbf{z})=p_\ell(\mathbf{z})\chi_{\mathbb{R}^n\setminus\overline{B}_\varepsilon}(\mathbf{z})+q_{\ell,\varepsilon}(\mathbf{z}),$$

where u_ℓ and p_ℓ solve (A.1) and (A.5) with $\Omega_i=\emptyset$. Changing variables $\boldsymbol{\xi}:=(\mathbf{z}-\mathbf{x})/\varepsilon$ the correction $v_{\ell,\varepsilon}(\boldsymbol{\xi},t)$ satisfies

$$\begin{cases} \Delta_\xi v_{\ell,\varepsilon} = a_e(\xi) & \text{in } \mathbb{R}^n \setminus \overline{B}, \\ \alpha_i \Delta_\xi v_{\ell,\varepsilon} = a_i(\xi) & \text{in } B, \\ v^-_{\ell,\varepsilon} - v^+_{\ell,\varepsilon} = b(\xi) & \text{on } \Gamma, \\ \alpha_i \mathbf{n}(\xi)\nabla_\xi v^-_{\ell,\varepsilon} - \mathbf{n}(\xi)\nabla_\xi v^+_{\ell,\varepsilon} = c(\xi) & \text{on } \Gamma \end{cases} \tag{A.10}$$

plus the Sommerfeld condition at infinity, with

$$a_\ell(\xi) = -\varepsilon^2 \lambda^2_{s_{\ell,e}} v_{\ell,\varepsilon}(\xi), \quad \ell = e, i,$$
$$b(\xi) = u_\ell(\mathbf{x}) + \varepsilon \xi \cdot \nabla u_\ell(\mathbf{x}, t) + \mathrm{O}(\varepsilon^2),$$
$$c(\xi, t) = \varepsilon \mathbf{n}(\xi) \cdot \nabla u_\ell(\mathbf{x}) + \mathrm{O}(\varepsilon^2).$$

B denotes the unit ball. Let us expand now $v_{\ell,\varepsilon}(\xi)$ in powers of ε : $v_{\ell,\varepsilon}(\xi) = v^{(1)}_\ell(\xi) + \varepsilon v^{(2)}_\ell(\xi) + \mathrm{O}(\varepsilon^2)$. The leading term of the expansion $v^{(1)}$ solves (A.10) with $a_e = a_i = c = 0$, $b = u_\ell(\mathbf{x})$, and $V^{(2)}$ solves (A.10) with $a_e = a_i = 0$, $b = \xi \cdot \nabla u(\mathbf{x})$, $c = \xi \cdot \nabla u(\mathbf{x})/|\xi|$. By inspection, $v^{(1)}_\ell(\xi) = u_\ell(\mathbf{x})\chi_B(\xi)$. Since $\Omega_i = \emptyset$, the total field is simply $u_\ell(\mathbf{x}) = u_{\mathrm{inc},\ell}(\mathbf{x})$. In dimension 2, the second term, $v^{(2)}_\ell(\xi)$, is found working in polar coordinates:

$$v^{(2)}_\ell(\xi) = \nabla u_\ell(\mathbf{x}) \left(\frac{2}{1+\alpha_i} \xi \chi_B(\xi) + \frac{1-\alpha_i}{1+\alpha_i} \frac{\xi}{|\xi|^2} \chi_{\mathbb{R}^2 \setminus \overline{B}}(\xi) \right) = \nabla u_\ell(\mathbf{x}) g(\xi). \tag{A.11}$$

Performing a similar expansion for $p_{\ell,\varepsilon}(\mathbf{z})$, we get

$$p_{\ell,\varepsilon}(\mathbf{z}) = p_\ell(\mathbf{z})\chi_{\mathbb{R}^n \setminus \overline{B}_\varepsilon}(\mathbf{z}) + p_\ell(\mathbf{x})\chi_{B_\varepsilon}(\mathbf{z}) + \varepsilon \nabla p_\ell(\mathbf{x}) g(\xi) + \mathrm{O}(\varepsilon^2), \quad \mathbf{z} \in \Gamma_\varepsilon.$$

This implies that

$$u_{\ell,\varepsilon}(\mathbf{z}) \to u_\ell(\mathbf{x}), \;\; p_{\ell,\varepsilon}(\mathbf{z}) \to p_\ell(\mathbf{x}) \quad \text{as } \varepsilon \to 0,$$

uniformly when $|\mathbf{z} - \mathbf{x}| = \varepsilon$. Expanding the derivatives we find

$$\frac{\partial u^-_{\ell,\varepsilon}}{\partial z_j}(\mathbf{z}) = \frac{\partial v^{(2)-}_\ell}{\partial \xi_j}(\xi, t) + \mathrm{O}(\varepsilon) = \frac{2}{1+\alpha_i} \frac{\partial u_\ell}{\partial z_j}(\mathbf{x}) + \mathrm{O}(\varepsilon)$$

and a similar identity for $p_{\ell,\varepsilon}$. Therefore

$$\nabla u^-_{\ell,\varepsilon}(\mathbf{z}) \to \frac{2}{1+\alpha_i} \nabla u_\ell(\mathbf{x}), \;\; \nabla p^-_{\ell,\varepsilon}(\mathbf{z}) \to \frac{2}{1+\alpha_i} \nabla p_\ell(\mathbf{x}) \quad \text{as } \varepsilon \to 0.$$

In dimension 3, we obtain an analogous expression to (A.11) working with spherical harmonics. Arguing as before it follows that

$$u_{\ell,\varepsilon}(\mathbf{z}) \to u_\ell(\mathbf{x}), \;\; p_{\ell,\varepsilon}(\mathbf{z}) \to p_\ell(\mathbf{x}) \quad \text{as } \varepsilon \to 0,$$
$$\nabla u^-_{\ell,\varepsilon}(\mathbf{z}) \to \frac{3}{2+\alpha_i} \nabla u_\ell(\mathbf{x}), \;\; \nabla p^-_{\ell,\varepsilon}(\mathbf{z}) \to \frac{3}{2+\alpha_i} \nabla p_\ell(\mathbf{x}) \quad \text{as } \varepsilon \to 0.$$

Step 6: Topological derivative in exterior domains. Let us calculate now the topological derivative of the cost functional (5) in $\mathcal{R} = \mathbb{R}^n \setminus \overline{\Omega}$. We argue as in Step 5, with slight changes in the expansions. Now, u_ℓ and p_ℓ solve forward and adjoint problems with $\Omega_i = \Omega$. (A.10) is replaced by a similar problem with $(\mathbb{R}^n \setminus \overline{B \cup \Omega_\varepsilon})$ and $B \cup \Omega_\varepsilon$ as exterior and interior domains, respectively, and zero transmission conditions on the new boundary $\partial\Omega_\varepsilon$, $\Omega_\varepsilon := (\Omega - \mathbf{x})/\varepsilon$.We just have to check that the presence of Ω_ε does not provide corrections to the orders zero and one. Expanding $v_{\ell,\varepsilon}(\xi)$ in powers of ε, the leading terms $v^{(1)}_\ell(\xi)$, $v^{(2)}_\ell(\xi)$ are the same as in Step 5. Furthermore, $v^{(1)}_\ell(\xi)$ is still an exact solution and $v^{(2)}_\ell(\xi)$ solves the corresponding equations with an error of order ε^2. Thus, the correction coming from Ω_ε appears at orders higher than ε, see [7,8] for more details on this type of expansions.

Step 7: Several time measurements. Finally, we define the function

$$p_{s_\ell}(\mathbf{x}) := \sum_{j=1}^{N} f(t_j) c_\ell \mathrm{e}^{t_j s_\ell} \bar{p}_\ell^j(\mathbf{x}),$$

where $\bar{p}_\ell^j$ solves (A.5). Then, by linearity it is straightforward to check that p_{s_ℓ} solves (22) and that the topological derivative of the cost functional (20) written in terms of p_{s_ℓ} is given by the identity (21).

Appendix B. Derivation of the topological derivative for the time-dependent problem

In this appendix, we prove Theorem 5.1. A number of nontrivial technical problems arise due to the singular nature of the incident and adjoint fields. For incident fields of the form (4), $U_{\mathrm{inc}}(0) = \delta_{\mathbf{x}_0}$. We first derive (28) for a sequence of incident fields U_{inc}^η, $U_{\mathrm{inc}}^\eta(0)$ being a sequence of functions of compact support tending to $\delta_{\mathbf{x}_0}$ as $\eta \to \infty$. The result follows then for our choice of U_{inc} in the limit $\eta \to \infty$. If $g \geqslant 0$ is a smooth function with compact support and $\int_{\mathbb{R}^2} g(\mathbf{x})\mathrm{d}\mathbf{x} = 1$, we take $U_{\mathrm{inc}}^\eta(0) = \frac{1}{\eta^2} g(\eta(\mathbf{x} - \mathbf{x}_0))$. The proof for such regularized incident fields is divided in several steps, following the ideas of Appendix A:

Step 1: Transformed functionals. To simplify, we will drop the subscript 'total' and the superscript η and rename as U the total field $U = U + U_{\mathrm{inc}}$ outside Ω_i and $U = U$ inside Ω_i, where U at the right-hand sides solves (6). The total field satisfies (6) with zero transmission conditions and initial datum U_{inc} in Ω_e. Since $U_{\mathrm{inc}}(0) \in W^{2,1}(\mathbb{R}^2) \cap W^{2,\infty}(\mathbb{R}^2)$, it follows that $U \in C^1([0,T] \times \Omega_i)$, $U \in C^1([0,T] \times \Omega_e)$, $U \in C([0,T]; H^2(\mathbb{R}^2))$ and $U_t \in C([0,T]; L^2(\mathbb{R}^2))$. Multiplying by a test function V and integrating over $[0,T] \times \mathbb{R}^2$, we obtain $b(\Omega_i; U, V) = 0$ where

$$b(\Omega_i; U, V) := \int_0^T \int_{\Omega_e} \left(\nabla U \nabla V + \frac{1}{\kappa_e} U_t V \right) \mathrm{d}\mathbf{z}\,\mathrm{d}s + \int_0^T \int_{\Omega_i} \left(\alpha_i \nabla U \nabla V + \frac{1}{\kappa_i} U_t V \right) \mathrm{d}\mathbf{z}\,\mathrm{d}s. \tag{B.1}$$

We deform the domains Ω_i as in Appendix A. The transformed cost functional is

$$J(\Omega_{i,\tau}) = \frac{1}{2} \sum_{j=1}^{N} f(t_j) \int_{\Gamma_{\mathrm{meas}}} (U_\tau(\mathbf{x}, t_j) - U_{\mathrm{meas}}(\mathbf{x}, t_j))^2 \mathrm{d}l_{\mathbf{z}}, \tag{B.2}$$

where U_τ satisfies $b(\Omega_{i,\tau}; U_\tau, V) = 0$, and $U_\tau(0) = U_{\mathrm{inc}}(0)\chi_{\Omega_e}$.
One might think of integrating by parts in time in (B.1) to obtain the standard variational formulation for the evolution problem, which includes a linear form defined in terms of the initial data on the right-hand side. This is not possible because when $V = P$ is our adjoint field (29), the integrals in time and space of UP_t diverge due to singularities at the observation times.
Step 2: Adjoint states. We define a modified functional

$$\mathcal{L}(\Omega_{i,\tau}; V, P) := J(\Omega_{i,\tau}) + b(\Omega_{i,\tau}; V, P)$$

for any V, P for which it makes sense. Then, the shape derivative of J in the direction $\mathbf{V}$ is

$$\begin{aligned} DJ(\Omega_i) \cdot \mathbf{V} &= \frac{\mathrm{d}}{\mathrm{d}\tau} \mathcal{L}(\Omega_{i,\tau}; U_\tau, P)\Big|_{\tau=0} \\ &= \frac{\mathrm{d}}{\mathrm{d}\tau} b(\Omega_{i,\tau}; U, P)\Big|_{\tau=0} + b(\Omega_i; \dot{U}, P) + \sum_{j=1}^{N} f(t_j) \int_{\Gamma_{\mathrm{meas}}} (U(\mathbf{x}, t_j) - U_{\mathrm{meas}}(\mathbf{x}, t_j)) \dot{U}(\mathbf{x}, t_j) \mathrm{d}l_{\mathbf{x}}. \end{aligned} \tag{B.3}$$

If we select a particular state P satisfying

$$b(\Omega_i; V, P) = -\sum_{j=1}^{N} f(t_j) \int_{\Gamma_{\mathrm{meas}}} (U(\mathbf{x}, t_j) - U_{\mathrm{meas}}(\mathbf{x}, t_j)) V(\mathbf{x}, t_j) \mathrm{d}l_{\mathbf{x}} \tag{B.4}$$

for $V = \dot{U}$, the shape derivative $DJ(\Omega)\cdot\mathbf{V}$ is given by the first term in the right-hand side of (B.3). Since our regularized U_{inc} has compact support about $\mathbf{x}_0$, we may assume that its support does not intersect Ω_i (take η large enough) and $\dot{U}_\tau(0) = 0$. Let us consider the solution P of

$$\begin{cases} -P_t - \kappa_e \Delta P = f(t)(U_{\text{meas}}(\mathbf{x},t) - U_{\text{total}}(\mathbf{x},t))\delta_{\Gamma_{\text{meas}}}(\mathbf{x})\sum_{j=1}^{N}\delta_{t_j}(t) \quad \text{in } \Omega_e\times[0,T],\\ -P_t - \alpha_i\kappa_i\Delta P = 0 \quad \text{in } \Omega_i\times[0,T],\\ P^- - P^+ = 0 \quad \text{on } \Gamma\times[0,T],\\ \alpha_i\partial_{\mathbf{n}}P^- - \partial_{\mathbf{n}}P^+ = 0 \quad \text{on } \Gamma\times[0,T],\\ P(\cdot,T) = 0 \quad \text{in } \mathbb{R}^2. \end{cases} \tag{B.5}$$

If we multiply these equations by $V = \dot{U}$, integrate by parts in t and $\mathbf{x}$ over $([\varepsilon, t_1-\varepsilon]\cup(\cup_{j=1}^{N}[t_j+\varepsilon, t_{j+1}-\varepsilon]))\times\mathbb{R}^2$, and let $\varepsilon\to 0$, (B.4) follows.

Step 3: Shape derivative. Let us calculate the first term in (B.3) for our choice of the adjoint field. For $U, P\in H$

$$\begin{aligned}\frac{\mathrm{d}}{\mathrm{d}\tau}b(\Omega_{i,\tau};U,P)\Big|_{\tau=0} &= \int_0^T\int_{\Omega_e}\left[\left(\nabla U\nabla P + \frac{1}{\kappa_e}U_tP\right)\operatorname{div}\mathbf{V} - ((\nabla\mathbf{V}+\nabla\mathbf{V}^\top)\nabla U)\nabla P\right]\mathrm{d}\mathbf{z}\,\mathrm{d}s\\ &\quad + \int_0^T\int_{\Omega_i}\left[\left(\alpha_i\nabla U\nabla P + \frac{1}{\kappa_i}U_tP\right)\operatorname{div}\mathbf{V} - \alpha_i((\nabla\mathbf{V}+\nabla\mathbf{V}^\top)\nabla U)\nabla P\right]\mathrm{d}\mathbf{z}\,\mathrm{d}s.\end{aligned} \tag{B.6}$$

Integrating by parts with respect to $\mathbf{x}$, recalling that $\mathbf{n}$ points inside Ω_i and using the transmission boundary conditions, we find

$$\begin{aligned}DJ(\Omega_i)\cdot\mathbf{V} &= \int_0^T\int_\Gamma\left[-\frac{1}{\kappa_i}+\frac{1}{\kappa_e}\right]U_tPV_n\,\mathrm{d}l\,\mathrm{d}s + \int_0^T\int_\Gamma[\alpha_i(1-\alpha_i)\partial_{\mathbf{n}}U^-\partial_{\mathbf{n}}P^- + (1-\alpha_i)\partial_{\mathbf{t}}U^-\partial_{\mathbf{t}}P^-]V_n\,\mathrm{d}l\,\mathrm{d}s\\ &\quad - \int_0^T\int_{\Omega_i}\left[\left(\alpha_i\Delta U + \frac{1}{\kappa_i}U_t\right)(\nabla P\cdot\mathbf{V}) + \alpha_i\Delta P(\nabla U\cdot\mathbf{V}) + \frac{1}{\kappa_i}P(\nabla U_t\cdot\mathbf{V})\right]\mathrm{d}\mathbf{z}\,\mathrm{d}s\\ &\quad - \int_0^T\int_{\Omega_e}\left[\left(\Delta U + \frac{1}{\kappa_e}U_t\right)(\nabla P\cdot\mathbf{V}) + \Delta P(\nabla U\cdot\mathbf{V}) + \frac{1}{\kappa_e}P(\nabla U_t\cdot\mathbf{V})\right]\mathrm{d}\mathbf{z}\,\mathrm{d}s.\end{aligned} \tag{B.7}$$

Unlike the time-harmonic or Laplace cases, the volume integrals now do not vanish. $\partial_{\mathbf{t}}$ stands for the tangent derivative.

Step 4: Topological derivative in the whole space. Once the shape derivative is known, the topological derivative is the limit

$$D_T(\mathbf{x},\mathbb{R}^2) = \lim_{\varepsilon\to 0}\frac{1}{\mathcal{V}'(\varepsilon)|V_n|}DJ(B_\varepsilon)\cdot\mathbf{V}_\varepsilon, \tag{B.8}$$

where $DJ(B_\varepsilon)\cdot\mathbf{V}_\varepsilon$ is given by (B.7) with Ω_i replaced by $B_\varepsilon = B_\varepsilon(\mathbf{x})$, Γ replaced by $\Gamma_\varepsilon = \partial B_\varepsilon(\mathbf{x})$ and U, P replaced by U_ε and P_ε. U_ε solves the forward problem (6) when $\Omega_i = B_\varepsilon(\mathbf{x})$ and P_ε solves (B.5) with $\Omega_i = B_\varepsilon$.By choice, $\mathbf{V}_\varepsilon\cdot\mathbf{n} = V_n < 0$ on Γ_ε. The integrals on B_ε integrate functions which depend on ε, but are bounded, over a region whose measure scales like ε^2. The singularities at t_j disappear splitting the time integral in intervals centered about t_j and making the changes of variables $\frac{\mathbf{x}-\mathbf{x}_k}{(t_j-t)^{1/2}}$ in space. The integrals on $\mathbb{R}^2\setminus\overline{B_\varepsilon}$ vanish out of a narrow neighborhood of B_ε by choice of $\mathbf{V}_\varepsilon$. Again we integrate bounded functions of $\mathbf{x}$, t and ε over a region whose measure scales like ε^2. If we divide by $\mathcal{V}'(\varepsilon) = 2\pi\varepsilon$ and let $\varepsilon\to 0$, the contribution of the volume integrals vanishes.The limit of the surface integrals is computed using asymptotic expansions of U_ε, P_ε in terms of the forward and adjoint solutions for $\Omega_i = \emptyset$, U and P:

$$U_\varepsilon(\mathbf{z},t) = U(\mathbf{z},t)\chi_{\mathbb{R}^2\setminus\overline{B}_\varepsilon}(\mathbf{z}) + V_\varepsilon(\mathbf{z},t), \quad P_\varepsilon(\mathbf{z},t) = P(\mathbf{z},t)\chi_{\mathbb{R}^2\setminus\overline{B}_\varepsilon}(\mathbf{z}) + Q_\varepsilon(\mathbf{z},t)$$

and expanding the remainders in powers of ε.

For our incident fields, $U_{\text{inc}}(0)$ has a narrow compact support about $\mathbf{x}_0$. We fix any point $\mathbf{x}$ for which $U_{\text{inc}}(\mathbf{x},0) = 0$.

Let us denote by B the unit ball. Performing the change of variables $\boldsymbol{\xi} := (\mathbf{z}-\mathbf{x})/\varepsilon$, the correction $V_\varepsilon(\boldsymbol{\xi},t)$ satisfies for $t \leqslant T$:

$$\begin{cases} \Delta_{\xi} V_\varepsilon = a_e(\boldsymbol{\xi},t) & \text{in } \mathbb{R}^2 \setminus \overline{B}, \\ \alpha_i \Delta_{\xi} V_\varepsilon = a_i(\boldsymbol{\xi},t) & \text{in } B, \\ V_\varepsilon^- - V_\varepsilon^+ = b(\boldsymbol{\xi},t) & \text{on } \Gamma, \\ \alpha_i \mathbf{n}(\xi)\nabla_{\xi} V_\varepsilon^- - \mathbf{n}(\boldsymbol{\xi})\nabla_{\xi} V_\varepsilon^+ = c(\boldsymbol{\xi},t) & \text{on } \Gamma, \\ V_\varepsilon(\cdot,0) = 0 & \text{in } \mathbb{R}^2 \end{cases} \tag{B.9}$$

with

$$a_\ell(\boldsymbol{\xi},t) = \frac{\varepsilon^2}{\kappa_e} V_{\varepsilon,t}(\boldsymbol{\xi},t), \quad \ell = e,i,$$
$$b(\boldsymbol{\xi},t) = U(\mathbf{x},t) + \varepsilon\boldsymbol{\xi}\cdot\nabla U(\mathbf{x},t) + \mathrm{O}(\varepsilon^2),$$
$$c(\boldsymbol{\xi},t) = \varepsilon\mathbf{n}(\boldsymbol{\xi})\cdot\nabla U(\mathbf{x},t) + \mathrm{O}(\varepsilon^2).$$

Let us expand now $V_\varepsilon(\boldsymbol{\xi},t)$ in powers of ε : $V_\varepsilon(\boldsymbol{\xi},t) = V^{(1)}(\boldsymbol{\xi},t) + \varepsilon V^{(2)}(\boldsymbol{\xi},t) + \mathrm{O}(\varepsilon^2)$. The leading term of the expansion $V^{(1)}$ solves (B.9) with $a_e = a_i = c = 0$, $b = U(\mathbf{x},t)$, and $V^{(2)}$ solves (B.9) with $a_e = a_i = 0$, $b = \boldsymbol{\xi}\cdot\nabla u(\mathbf{x},t)$, $c = \boldsymbol{\xi}\cdot\nabla u(\mathbf{x},t)$. Notice that $\mathbf{n}(\boldsymbol{\xi}) = \boldsymbol{\xi}$.
By inspection, $V^{(1)}(\boldsymbol{\xi},t) = U(\mathbf{x},t)\chi_B(\boldsymbol{\xi})$. Notice that $U_{\mathrm{inc}}(\mathbf{x},0) = 0$. This guarantees that $V^{(1)}$ satisfies the initial condition. The second term, $V^{(2)}(\boldsymbol{\xi},t)$, is found working in polar coordinates:

$$V^{(2)}(\boldsymbol{\xi},t) = \nabla U(\mathbf{x},t)\left(\frac{2}{1+\alpha_i}\boldsymbol{\xi}\chi_B(\boldsymbol{\xi}) + \frac{1-\alpha_i}{1+\alpha_i}\frac{\boldsymbol{\xi}}{|\boldsymbol{\xi}|^2}\chi_{\mathbb{R}^2\setminus\overline{B}}(\boldsymbol{\xi})\right) = \nabla U(\mathbf{x},t) g(\boldsymbol{\xi}).$$

Again, the fact that $U_{\mathrm{inc}}(\mathbf{x},0) = 0$ guarantees that the initial condition is satisfied. Under this assumption:

$$U_\varepsilon(\mathbf{z},t) = U(\mathbf{z},t)\chi_{\mathbb{R}^2\setminus\overline{B}_\varepsilon}(\mathbf{z}) + U(\mathbf{x},t)\chi_{B_\varepsilon}(\mathbf{z}) + \varepsilon\nabla U(\mathbf{x},t) g(\boldsymbol{\xi}) + \mathrm{O}(\varepsilon^2), \quad \mathbf{z}\in\Gamma_\varepsilon.$$

Performing a similar expansion for $P_\varepsilon(\mathbf{z})$, we get

$$P_\varepsilon(\mathbf{z},t) = P(\mathbf{z},t)\chi_{\mathbb{R}^2\setminus\overline{B}_\varepsilon}(\mathbf{z}) + P(\mathbf{x},t)\chi_{B_\varepsilon}(\mathbf{z}) + \varepsilon\nabla P(\mathbf{x},t) g(\boldsymbol{\xi}) + \mathrm{O}(\varepsilon^2), \quad \mathbf{z}\in\Gamma_\varepsilon.$$

This implies that

$$U_\varepsilon(\mathbf{z},t) \to U(\mathbf{x},t), \qquad P_\varepsilon(\mathbf{z},t) \to P(\mathbf{x},t) \quad \text{as } \varepsilon\to 0,$$

uniformly when $|\mathbf{z}-\mathbf{x}| = \varepsilon$ and $0 \leqslant t \leqslant T$. Expanding the derivatives we find

$$\frac{\partial U_\varepsilon^-}{\partial z_j}(\mathbf{z},t) = \varepsilon\frac{\partial V^{(2)-}}{\partial z_j}(\boldsymbol{\xi},t) + \mathrm{O}(\varepsilon) = \frac{2}{1+\alpha_i}\frac{\partial U}{\partial z_j}(\mathbf{x},t) + \mathrm{O}(\varepsilon)$$

and a similar identity for P_ε. Therefore

$$\nabla U_\varepsilon^-(\mathbf{z},t) \to \frac{2}{1+\alpha_i}\nabla U(\mathbf{x},t), \quad \nabla P_\varepsilon^-(\mathbf{z},t) \to \frac{2}{1+\alpha_i}\nabla P(\mathbf{x},t) \quad \text{as } \varepsilon\to 0.$$

Analogous arguments show that the time derivatives of $U_{\varepsilon,t}$, $P_{\varepsilon,t}$ tend to the time derivatives U_t, P_t. Notice that $U_t(\mathbf{x},0) = \Delta U(\mathbf{x},0) = 0$ and $P_t(\mathbf{x},T) = \Delta P(\mathbf{x},T) = 0$. Taking limits in the surface integrals, we find (28) for any $\mathbf{x}$ outside the support of $U_{\mathrm{inc}}(0)$.

References

[1] D.P. Almond, P.M. Patel, Photothermal Science and Techniques, Chapman and Hall, London, 1996.
[2] H.T. Banks, F. Kojima, Boundary shape identification problems in two-dimensional domains related to thermal testing of materials, Quart. Appl. Math. 47 (1989) 273–293.

[3] H.T. Banks, F. Kojima, W.P. Winfree, Boundary estimation problems arising in thermal tomography, Inverse Probl. 6 (1990) 897–921.
[4] G. Beylkin, Imaging of discontinuities in the inverse scattering problem by inversion of causal generalized Radon transform, J. Math. Phys. 26 (1985) 99–108.
[5] M. Burger, B. Hackl, W. Ring, Incorporating topological derivatives into level set methods, J. Comput. Phys. 194 (2004) 344–362.
[6] F. Cakoni, D. Colton, P. Monk, The determination of the surface conductivity of a partially coated dielectric, SIAM J. Appl. Math. 65 (2005) 767–789.
[7] A. Carpio, M.-L. Rapún, Solving inhomogeneous inverse problems by topological derivative methods, Inverse Probl., On line at stacks.iop.org/IP/24/045014, doi:10.1088/0266-5611/24/4/045014.
[8] A. Carpio, M.-L. Rapún, Topological derivatives for shape reconstruction, in: Inverse Problems and Imaging, Lecture Notes in Mathematics, Springer, 2008, pp. 85–134.
[9] M. Cheney, D. Isaacson, J.C. Newell, Electrical impedance tomography, SIAM Rev. 41 (1999) 85–101.
[10] M. Costabel, E. Stephan, A direct boundary integral equation method for transmission problems, J. Math. Anal. Appl. 106 (1985) 367–413.
[11] O. Dorn, D. Lesselier, Level set methods for inverse scattering, Inverse Probl. 22 (2006) R67–R131.
[12] L. Elden, F. Berntsson, T. Reginska, Wavelet and Fourier methods for solving the sideways heat equation, SIAM J. Sci. Comput. 21 (2000) 2187–2205.
[13] G.R. Feijoo, A new method in inverse scattering based on the topological derivative, Inverse Probl. 20 (2004) 1819–1840.
[14] F. Garrido, A. Salazar, Thermal wave scattering from spheres, J. Appl. Phys. 95 (2004) 140–149.
[15] B.B. Guzina, M. Bonnet, Topological derivative for the inverse scattering of elastic waves, Quart. J. Mech. Appl. Math. 57 (2004) 161–179.
[16] B.B. Guzina, M. Bonnet, Small-inclusion asymptotic of misfit functionals for inverse problems in acoustics, Inverse Probl. 22 (2006) 1761–1785.
[17] D.M. Heath, C.S. Welch, W.P. Winfree, Quantitative thermal diffusivity measurements of composites, Review of Progress in Quantitative Non-Destructive Evaluation, vol. 5B, Plenum, New York, 1986, pp. 1125–1132.
[18] T. Hohage, M.-L. Rapún, F.-J. Sayas, Detecting corrosion using thermal measurements, Inverse Probl. 23 (2007) 53–72.
[19] T. Hohage, F.-J. Sayas, Numerical approximation of a heat diffusion problem by boundary element methods using the Laplace transform, Numer. Math. 102 (2005) 67–92.
[20] V. Isakov, Inverse Problems for Partial Differential Equations, Springer, New York, 1998.
[21] A. Laliena, F.-J. Sayas, LDBEM in diffusion problems, in: Proceedings of XIX CEDYA/IX CMA, 2005 (electronic version).
[22] M. López-Fernández, C. Palencia, On the numerical inversion of the Laplace transform of certain holomorphic mappings, Appl. Numer. Math. 51 (2004) 289–303.
[23] A. Mandelis, Diffusion-wave fields. Mathematical methods and Green functions, Springer, New York, 2001.
[24] A. Mandelis, Diffusion waves and their uses, Phys. Today 53 (2000) 29–34.
[25] L. Nicolaides, A. Mandelis, Image-enhanced thermal-wave slice diffraction tomography with numerically simulated reconstructions, Inverse Probl. 13 (1997) 1393–1412.
[26] A. Ocáriz, A. Sánchez-Lavega, A. Salazar, Photothermal study of subsurface cylindrical structures: II. Experimental results, J. Appl. Phys. 81 (1997) 7561–7566.
[27] M.A. O'Leary, D.A. Boas, B. Chance, A.G. Yodh, Refraction of diffusive photon density waves, Phys. Rev. Lett. 69 (1992) 2658–2662.
[28] M.-L. Rapún, F.-J. Sayas, Boundary integral approximation of a heat diffusion problem in time-harmonic regime, Numer. Algor. 41 (2006) 127–160.
[29] M.-L. Rapún, F.-J. Sayas, Boundary element simulation of thermal waves, Arch. Comput. Methods Eng. 14 (2007) 3–46.
[30] A. Salazar, A. Sánchez-Lavega, R. Celorrio, Scattering of cylindrical thermal waves in fiber composites: in-plane thermal diffusivity, J. Appl. Phys. 93 (2003) 4536–4542.
[31] A. Talbot, The accurate numerical inversion of Laplace transforms, J. Inst. Math. Appl. 23 (1979) 97–120.
[32] J.M. Terrón, A. Salazar, A. Sánchez-Lavega, General solution for the thermal wave scattering in fiber composites, J. Appl. Phys. 91 (2002) 1087–1098.